ISSN 0915-633X

NATIONAL INSTITUTE FOR FUSION SCIENCE

Intensification of Magnetic Field by Concentrate-and-Stretch of Magnetic Flux Lines

H. Kitauchi and S. Kida

(Received - Aug. 19, 1997)

NIFS-506 Sep. 1997

RESEARCH REPORT
NIFS Series

NAGOYA, JAPAN

Intensification of Magnetic Field by Concentrate-and-Stretch of Magnetic Flux Lines

Hideaki Kitauchi and Shigeo Kida

Theory and Computer Simulation Center, National Institute for Fusion Science, Oroshi-cho 322-6, Toki, 509-52, Japan

Abstract

The mechanism of generation of magnetic field by thermal convection is investigated by analyzing the numerical solution to the Boussinesq magneto-hydrodynamic equations in a rotating spherical shell. The magnetic flux lines are intensified by concentrate-and-stretch around sinks in the outer boundary layer, on the equatorial plane and in the inner boundary layer, and the strong magnetic field is generated downstream of them. The magnetic flux lines are being stretched there irrespective as to whether fluid elements accelerate or decelerate.

keywords: MHD dynamo, thermal convection, rotating spherical shell, concentrate-and-stretch.

I. INTRODUCTION

The mechanism of geodynamo is one of the unsolved fundamental problems in geophysics. It is generally believed that the magnetic field is generated by the motion of an electrically conducting fluid in the outer core. As described conceptually by Parker,[1] the toroidal magnetic field is converted from the poloidal by shearing motion of the non-uniform east-west fluid flows. The latter, on the other hand, is converted back from the former by twisting motion of the upwelling or the downwelling helical fluid flows. This kinematic argument is

interesting but seems too simple to explain the observed structure of geomagnetic field and its temporal evolution even in a qualitative way.

Historically, the dynamo mechanism has been studied by solving the magneto-hydrodynamic (MHD) equations either kinematically or self-consistently (see Ref. 2 for a review). Roberts[3] discovered in his spherical kinematic dynamo models the condition of appearance of either an oscillatory or a steady magnetic field of either dipolar or quadrupolar structure, which depends on the type of the velocity field.

Accurate direct numerical simulations of the MHD equations in a rotating spherical shell have become possible only recently thanks to a rapid development of computer sciences. Kageyama and his co-workers[4] solved the compressible MHD equations by means of a finite difference scheme by imposing a symmetry with respect to the equatorial plane of the velocity and the magnetic fields, and observed an unsteady strong magnetic field of which the energy is one order of magnitude greater than the kinetic. In a different run[5,6] without imposing the above symmetry, they realized a steady dipole dynamo in which the magnetic energy was about twice as large as the kinetic, and interpreted the growth of the dipole magnetic field in terms of the so-called $\alpha\omega$ dynamo mechanism. Glatzmaier and Roberts[7] solved a set of modified Boussinesq MHD equations derived in the limit of large Taylor and Rayleigh numbers. They realized a strong magnetic field whose energy was three orders of magnitude greater than the kinetic, and observed a reversal of magnetic field. Kida et al.[8] solved the Boussinesq MHD equations by means of the spectral method to observe periodic reversals of magnetic field, in which the magnetic energy was 30% of the kinetic.

In this paper we examine the generation mechanism of magnetic field driven by a thermal convection in a rotating spherical shell. The knowledge of the spatial structure of velocity field is prerequisite for the understanding of the mechanism. In a previous paper[9] we analyzed the detailed structure of thermal convection without magnetic field. Five pairs of cyclonic (i.e. rotating in the same sense as the spherical shell) and anti-cyclonic vortex columns drift westward steadily with constant angular velocity. We perform here an MHD simulation by adding a small random perturbation of magnetic field on this steady thermal

convection state. A special attention is paid to the spatial correlation between the magnetic and the velocity fields for the purpose of understanding of generation mechanism of magnetic field. The basic equations and the numerical method are briefly explained in §2. The numerical results are presented in §3, in which the spatio-temporal structure (§3.1) and the generation mechanism (§3.2) of magnetic field are discussed. Section 4 is devoted to our concluding remarks.

II. FORMULATIONS

We consider the interplay between the motion of an electrically conducting fluid and the temporal evolution of the magnetic field by solving numerically the MHD equations (see (1)–(5) below). A fluid of density ρ is confined in a spherical shell which is rotating with constant angular velocity $\boldsymbol{\Omega}$ (see figure 1). The inner and the outer boundaries of the shell are spheres of radii r_1 and $r_2(= r_1 + d)$, respectively. The temperature on each boundary is kept uniform over the sphere and constant at all the time. It is hotter on the inner sphere than on the outer by ΔT, which drives a thermal convection. The gravity force $\boldsymbol{g} = -\rho\gamma\boldsymbol{x}$ is assumed to work on fluid elements per unit volume, where γ is a constant and $\boldsymbol{x}$ is a position vector relative to the center of the system. It is also assumed, for simplicity, that there is vacuum outside the shell and that the magnetic permeability of the fluid is equal to that of vacuum.

Under the Boussinesq and the MHD approximations the equations of fluid motion and the magnetic field are written, in a frame rotating with the shell, as

$$\frac{\partial \boldsymbol{u}}{\partial t} = -\nabla P + P_r R_a T \boldsymbol{x} + \boldsymbol{u} \times (\nabla \times \boldsymbol{u}) - \boldsymbol{b} \times (\nabla \times \boldsymbol{b}) + P_r T_a^{\frac{1}{2}} \boldsymbol{u} \times \hat{\boldsymbol{z}} + P_r \nabla^2 \boldsymbol{u}, \tag{1}$$

$$\frac{\partial \boldsymbol{b}}{\partial t} = \nabla \times (\boldsymbol{u} \times \boldsymbol{b}) + R_o \nabla^2 \boldsymbol{b}, \tag{2}$$

$$\frac{\partial T}{\partial t} = -\nabla \cdot (\boldsymbol{u} T) + \nabla^2 T, \tag{3}$$

$$\nabla \cdot \boldsymbol{u} = 0, \tag{4}$$

$$\nabla \cdot \boldsymbol{b} = 0. \tag{5}$$

Here, $\boldsymbol{u}$ is the velocity, $P = p/\rho + \frac{1}{2}|\boldsymbol{u}|^2 + \frac{1}{2}\gamma|\boldsymbol{x}|^2 - \frac{1}{2}|\boldsymbol{\Omega} \times \boldsymbol{x}|^2$ is a modified pressure (p is the true pressure), T is the temperature, $\boldsymbol{b}$ is the magnetic flux density and $\hat{\boldsymbol{z}} = \boldsymbol{\Omega}/|\boldsymbol{\Omega}|$ is the unit vector along the rotation axis. All the variables have been normalized in terms of thickness d of the shell, thermal diffusion time d^2/κ (κ is the thermal diffusivity), temperature difference ΔT between the two boundaries and the magnetic flux density $\kappa(\mu\rho)^{\frac{1}{2}}/d$. There appear four dimensionless parameters,

$$P_r = \frac{\nu}{\kappa}, \quad R_a = \frac{\alpha\gamma\Delta T d^4}{\kappa\nu}, \quad T_a = \left(\frac{2|\boldsymbol{\Omega}|d^2}{\nu}\right)^2, \quad R_o = \frac{\lambda}{\kappa}, \tag{6}$$

which we call the Prandtl number, the Rayleigh number, the Taylor number and the Roberts number, respectively, where α is the thermal expansion coefficient, ν is the kinematic viscosity of fluid and λ is the electrical resistivity. The magnetic Prandtl number $P_m = \nu/\lambda$ is expressed as $P_m = P_r/R_o$.[†]

The no-slip boundary condition is imposed for the velocity field. The magnetic field inside and outside the shell is connected smoothly on the boundaries. Equations (1)–(5) with these boundary conditions are solved numerically by the pseudo-spectral method described in Ref. 8. The simulation is performed in two steps. First, a steady thermal convection state is realized in a run without magnetic field with parameters,

$$R_a = 3200, \quad T_a = 8000, \quad P_r = 1, \quad r_1/r_2 = 0.5, \tag{7}$$

in which five pairs of cyclonic and anti-cyclonic vortex columns drift westward steadily with angular velocity $\Omega_V \approx 1.2$.[9] Thin boundary layers, what is called the Ekman layers, are developed on both the inner and the outer spheres. An MHD simulation is then carried out by adding a small random seed of magnetic field to the above steady thermal convection

[†]Prandtl number P_m in Ref. 8 should be read as Roberts number R_o.

state. Several runs with different values of R_o are performed. It turns out that the magnetic field is generated for $R_o < 0.122$. In the following we will report a near-critical case with $R_o = 0.12$.

III. RESULTS

A. Temporal Evolution and Spatial Structure of Magnetic Field

The growth of the magnetic field is most conveniently monitored by the total magnetic energy

$$\mathcal{E}_M(t) = \int_V \tfrac{1}{2}|\boldsymbol{b}(\boldsymbol{x},t)|^2 d\boldsymbol{x}, \tag{8}$$

where the integration is taken over the whole space. The temporal evolution of $\mathcal{E}_M$ is shown in figure 2 together with the kinetic energy

$$\mathcal{E}_K(t) = \int_V \tfrac{1}{2}|\boldsymbol{u}(\boldsymbol{x},t)|^2 d\boldsymbol{x}. \tag{9}$$

It is seen that the magnetic energy increases at first exponentially in time and saturates around $t = 300$ to about 11.206 accompanied with an oscillation of very small amplitude ($\approx 10^{-3}$) and a period of about 16 (see figures 2 (b) and 4 (c-i)). The kinetic energy, on the other hand, remains almost constant over the whole period. The total magnetic energy is about 2% of the kinetic in this quasi-steady state. The magnetic energies inside the inner boundary and outside the outer are only about 0.5% and 5% of the total, respectively.

The symmetry of the system with respect to the equatorial plane allows two purely symmetric states. The magnetic field can be either symmetric or anti-symmetric, while the velocity and the temperature fields are restricted to be symmetric. In the present simulation a purely anti-symmetric magnetic field happens to be realized even starting with an asymmetric random initial condition.

One of the most interesting physical quantities which characterize the dynamo action in a rotating system is a magnetic dipole moment

$$\boldsymbol{m}(t) = \int_V \tfrac{1}{2}\boldsymbol{x} \times \boldsymbol{j}(\boldsymbol{x}, t) d\boldsymbol{x}, \tag{10}$$

where $\boldsymbol{j} = \nabla \times \boldsymbol{b}$ is the electric current density.[†] The temporal evolution of the axial component m_z of the magnetic dipole moment is shown in figure 3. The cross component is negligible at all the time ($< 10^{-5}$). It stays nearly zero during the early period of the exponential growth of the magnetic energy ($t \leq 150$, see figure 2). Then, it starts to oscillate with increasing amplitude. The period of oscillation is about 32 ($= 16 \times 2$) in the quasi-steady state, which synchronizes with the oscillation of the total magnetic energy.

As stated in §2, the vortex columns drift westward steadily with angular velocity Ω_V, so that the flow field is steady in a frame rotating with this angular velocity. Notice that the outer and the inner boundaries move eastward in this steady-flow frame.

The temporal evolution of the spatial structure of magnetic field in the steady-flow frame is shown in figures 4, where the magnitude of magnetic flux density is depicted by blue iso-surface at the level of $|\boldsymbol{b}| = 2$ ($|\boldsymbol{b}|_{\max} = 3.4$), which are viewed (a) from the north pole and (b) from an oblique angle. They cover two periods of oscillation of $\mathcal{E}_M$ (or one period of oscillation of m_z). See figure 4 (c) for the temporal evolution of $\mathcal{E}_M$ and m_z in this period. Dark (or light) blue in figures 4 (a) and (b) implies that the z-component b_z of the magnetic flux density is positive (or negative). Transparent iso-surfaces of vorticity magnitude are drawn at $|\boldsymbol{\omega}| = 52$ in region $1.15r_1 \leq r \leq 0.91r_2$. The boundary layers on the outer and the inner spheres, in which the vorticity is very large, are removed for better representation.

There are several interesting features observed in these figures. First, the magnetic field is not five-fold symmetric around the rotation axis though the velocity field is. This asymmetric mode is shown by a linear stability analysis (or equivalently by a kinematic dynamo approach) to be more unstable than the symmetric one.[10] Second, the regions of

---

[†]In our previous paper,[8] we defined a dipole moment vector $\boldsymbol{P}$ in terms of the first order coefficients in the spherical harmonic expansion of the magnetic flux density outside the outer spherical boundary, which is related with $\boldsymbol{m}$ as $\boldsymbol{m} = -2\sqrt{6}\pi r_2^2 \boldsymbol{P}$.

strong magnetic field change in time in a peculiar way. In the first half of the period ((i)-(v)) the dark blue regions in the left are diminishing, while new regions of the same color are born in the right. During this process the light blue regions in the middle hardly change. In the second half ((v)-(ix)) the process is exactly the same as that in the first, but the direction of magnetic field is reversed. Incidentally, the structure of magnetic field in (ix) is identical to that in (i), but the location is shifted eastward by angle of $\frac{4}{5}\pi$. Third, the intense magnetic field is confined in three distinct domains, that is, around the tops of cyclones and their western neighbor anti-cyclones, inside the anti-cyclones, and between cyclones and their western neighbor anti-cyclones.

In order to extract the domains where the intense magnetic field is generated, we plot, in figure 5, the envelope surface of the magnitude of magnetic flux density, that is, the supreme at each point of $|\boldsymbol{b}|$ over time interval $385 \leq t \leq 433$ (three periods of oscillation of $\mathcal{E}_M$) at the level of $|\boldsymbol{b}| = 2$. They are viewed (a) from the north pole, (b) from an oblique angle and (c) from the equatorial plane. It is clear that the intense magnetic field is confined only in the three kinds of domains mentioned above. In the next subsection we scrutinize the intensification mechanism of magnetic field in these domains.

B. Mechanism of Magnetic Field Intensification

Since the intensification mechanism of magnetic field seems to be common at all the time, we examine it by analyzing the field at $t = 385$ (figures 4 (a-i) and (b-i)). As representative points of the three kinds of domains of intense magnetic field identified in the preceding section, we take local maxima of $|\boldsymbol{b}|$. Their positions in the respective domains, which are denoted by P1, P2 and P3, are plotted in figure 6. They are located in the vicinity of the outer sphere, the equatorial plane and the inner sphere, respectively. The local maxima at P1, P2 and P3 are 2.8, 2.8 and 2.5, respectively.

For a later convenience in the discussion of magnetic field intensification we write here the evolution equation of magnetic energy density, which is obtained by multiplying induction

equation (2) by $\boldsymbol{b}$,

$$\frac{\partial}{\partial t}\tfrac{1}{2}|\boldsymbol{b}|^2 = \boldsymbol{b}\cdot\underline{\boldsymbol{s}}\cdot\boldsymbol{b} - (\boldsymbol{u}\cdot\nabla)\tfrac{1}{2}|\boldsymbol{b}|^2 + R_o\boldsymbol{b}\cdot\left(\nabla^2\boldsymbol{b}\right), \tag{11}$$

where $\underline{\boldsymbol{s}}$ is the rate of strain tensor

$$\underline{\boldsymbol{s}} = \{s_{ij}\}, \quad s_{ij} = \left(\frac{\partial u_i}{\partial x_j} + \frac{\partial u_j}{\partial x_i}\right), \quad (i,j = 1,2,3). \tag{12}$$

The first term on the right-hand side of eq. (11) represents the magnetic field intensification (or weakening) through stretching (or shrinking) of magnetic flux lines by fluid motion. The second and the third terms represent the advection of magnetic energy density and the diffusion/dissipation by resistivity, respectively. These terms normalized by $\frac{1}{2}|\boldsymbol{b}|^2$ as

$$S = \frac{\boldsymbol{b}\cdot\underline{\boldsymbol{s}}\cdot\boldsymbol{b}}{\frac{1}{2}|\boldsymbol{b}|^2}, \quad A = \frac{-(\boldsymbol{u}\cdot\nabla)\frac{1}{2}|\boldsymbol{b}|^2}{\frac{1}{2}|\boldsymbol{b}|^2}, \quad D = \frac{R_o\boldsymbol{b}\cdot(\nabla^2\boldsymbol{b})}{\frac{1}{2}|\boldsymbol{b}|^2}, \tag{13}$$

which represent the contribution to the growth rate of the intensity of magnetic field, are called here the stretching, the advection, and the diffusion/dissipation terms, respectively. Note that this normalization is essential for the correct estimation of the contribution of the velocity field to the growth rate of the magnetic field. Otherwise, it is masked by the intensity of the magnetic field. In the following we discuss the intensification mechanism of magnetic field in the above three domains one by one.

1. *Around Tops of Cyclones and their western neighbor Anti-cyclones*

The magnetic flux lines around P1 which is located near a top of an anti-cyclone are shown in figure 7 (a). They pass a circle of radius 0.15 centered at P1 on a plane perpendicular to $\boldsymbol{b}$. They are drawn only inside the shell. It is seen that the magnetic flux lines run in parallel with the regions of high $|\boldsymbol{b}|$ and that they tend to be along the outer sphere in the boundary layer.

In order to see the flow structure which generates the magnetic field, we plot, in figure 7 (b), streamlines (in a frame moving with the vortex columns) projected on a sphere of radius $0.97r_2$ (at the fifth grid from the outer sphere in the calculation mesh) which is located near

the edge of the outer boundary layer. Here, the color represents the acceleration of fluid elements: red denotes positive and white negative The radial component u_r of the velocity is represented by contour lines as well as by color map. where dark blue implies positive and light blue negative. There are a single source around the north pole and five near the equator, whereas five sinks at the middle latitude. Those streamlines that flow out of the north pole split into five. Each of them spirals anti-clockwise into one of the five sinks. The streamlines which flow out of one of the sources near the equator split into two. They spiral anti-clockwise into either a western or an eastern neighbor sink. The fluid elements accelerate and decelerate around the sources and the sinks, respectively. The mean radial component of velocity is one order of magnitude smaller than that of the surface component on this sphere. The position of a sink does not necessarily coincide with a local minimum of u_r because the flow is not perpendicular to the sphere. A comparison of figure 7 (a) and (b) reveals that the intense magnetic flux region is rooted at the sink.

The three-dimensional structure of fluid motion is shown in figure 7 (c) with streamlines which are drawn from a circle of radius 0.2 centered at P1 on a plane perpendicular to the velocity vector. The meaning of the color is the same as that in figure 7 (b) . The streamlines which run in the outer boundary layer spiral anti-clockwise into the sink. The fluid elements decelerate near the sink in the outer boundary layer, but accelerate behind it inside the shell.

The spatial correlation between the velocity and the magnetic fields is clearly seen in figure 7 (d), in which the magnetic flux lines in figure 7 (a) and the streamlines in figure 7 (c) are superposed. Note, however, that the color of streamlines now represents the sign of stretching term S; red denotes positive and white negative. It is seen that the magnetic field is being intensified by concentrate-and-stretch of magnetic flux lines around the sink and that the intense magnetic field is generated downstream of it.

In order to examine the mechanism of intensification of magnetic field quantitatively, we show, in figure 8 (a), the variations of the stretching (S), advection (A) and diffusion/dissipation (D) terms along a streamline which passes P1. This is drawn in figure 7

(e), where the color of streamlines represents the sign of S, and P1U and P1D denote null points of S. The stretching term is positive between P1U and P1D. It is seen in figure 8 (a) that the stretching term dominates the other two near-upstream of P1, which implies that the magnetic field around P1 is being intensified by the stretching of magnetic flux lines.

The stretching of magnetic flux lines is closely related to the acceleration a of fluid motion and the angle $\vartheta_{\boldsymbol{b}}$ between the velocity and the magnetic flux vectors. Their variations along the streamline shown in figure 7 (e) are drawn together with $|\boldsymbol{b}|$ in figure 8 (b). Because the velocity field is solenoidal, the fluid elements are likely to be stretched along (or across) a streamline in the places where they accelerate (or decelerate). The fluid elements accelerate and the angle is smaller near-upstream of P1, whereas they decelerate and the angle is larger far-upstream. This may explain that the magnetic flux lines are stretched over the whole upstream of P1 irrespective as to whether fluid elements accelerate or decelerate. Those magnetic flux lines that pass the streamline between P1U and P1D are plotted in figure 7 (f). We see that the magnetic flux lines which are almost perpendicular to the streamline around P1U tend to align with it near P1.

2. Inside Anti-cyclones

The mechanism of intensification of magnetic field around P2 is similar to that around P1 discussed in the preceding subsection. In figures 9 and 10 we draw the same quantities as in figures 7 and 8 except for figure 9 (b) in which the contour lines and the color map are shown for $\partial u_z/\partial z$.

The magnetic flux lines around P2 are aligned in the north-south direction in an anti-cyclone (figure 9 (a)). These magnetic flux lines are situated around a spiral sink of the thermal convection in the equatorial plane. The streamlines around an anti-cyclone spiral clockwise into the center of it and expand in the north-south direction ($\partial u_z/\partial z > 0$) (figure 9 (b)). The flow around P2 makes a spiral upwelling motion in the anti-cyclone (figure 9 (c)). As shown in figure 9 (d), the magnetic field is being intensified by concentrate-and-stretch of

magnetic flux lines around the sink and that the intense magnetic field is generated behind it.

It is seen in figure 10 (a) that the stretching term dominates the other two near-upstream of P2 along a streamline which passes P2 (figure 9 (e)). This means that the magnetic field around P2 is being intensified by the stretching of magnetic flux lines. As a matter of fact, the magnetic flux lines which pass the streamline between P2U and P2D (figure 9 (f)) are stretched over the whole upstream of P2. They are stretched across the streamline far-upstream of P2, while along it near-upstream and downstream (figure 10 (b)).

3. Between Cyclones and their western neighbor Anti-cyclones

The mechanism of intensification of magnetic field around P3 is also similar to that around P1 and P2. We draw again, in figures 11 and 12, the same quantities as in figures 7 and 8.

As seen in the streamlines projected on a sphere of radius $1.06r_1$ which is located near the edge of the inner boundary layer (figure 11 (b)), there is a sink around the north pole and five pairs of sources and sinks near the equator. Those streamlines that flow out of one of the sources split into three. They run toward either a western, an eastern or the north polar sink. The fluid elements accelerate and decelerate around the sources and the sinks, respectively. The mean radial component of velocity is one order of magnitude smaller than that of the surface component on this sphere. The sinks near the equator are extended on lines in the inner boundary layer, which contrasts the point-like sinks in the outer boundary layer. The magnetic flux lines and the streamlines which start from two lines parallel to the line-sink on the both sides on this sphere are shown in figure 11 (a) and (c), respectively. They are concentrated in a sheet between a cyclone and its western neighbor anti-cyclone. We observe again, in figure 11 (d), that the magnetic field is concentrated toward the sink and intensified by stretching of magnetic flux lines and that the intense magnetic field is generated downstream of it.

As seen in figure 12, the behavior of the three terms in the magnetic energy density equation, the acceleration of fluid elements and the angle between the velocity and the magnetic field vectors are qualitatively same as those around P1 and P2. Incidentally, it may be attributed to the weak intensity of the sink at the north pole that the magnetic field there is not so strong.

IV. CONCLUDING REMARKS

By solving numerically the Boussinesq MHD equations in a rotating spherical shell, we have realized an anti-symmetric oscillatory dynamo in a symmetric quasi-steady convection. Since the Roberts number is just below the critical, the intensity of the generated magnetic energy is weak (about 2% of the kinetic energy) and does hardly disturb the velocity field. This makes it much easier to analyze the mechanism of the intensification of magnetic field.

The magnetic flux lines are convected and concentrated, while being stretched, toward sinks in the outer boundary layer, on the equatorial plane and in the inner boundary layer, and the intense magnetic field is generated downstream of them. It is interesting to note that the magnetic flux lines are stretched around the sink irrespective as to whether fluid elements accelerate or decelerate. This happens because of the change of the angle between the magnetic flux lines and the streamlines.

It may be also interesting to compare three kinds of stretching processes, i.e. the stretchings of the magnetic flux lines, the vorticity lines and the fluid elements. The temporal evolution of the total magnetic energy in the spherical shell is described by

$$\frac{d}{dt}\int_{shell}\tfrac{1}{2}|\boldsymbol{b}|^2 d\boldsymbol{x} = \int_{shell}\boldsymbol{b}\cdot\underline{\boldsymbol{s}}\cdot\boldsymbol{b}\,d\boldsymbol{x} + R_o\int_{shell}\boldsymbol{b}\cdot\left(\nabla^2\boldsymbol{b}\right)d\boldsymbol{x}, \tag{14}$$

which is obtained by integrating eq. (11). Note that the advection term has been integrated out. In the quasi-steady state ($t \geq 350$) the magnetic-flux-line stretching term gives a positive contribution which is balanced with the diffusion/dissipation one. As for vorticity, a *curl* of eq. (1) yields the vorticity equation

$$\frac{\partial \boldsymbol{\omega}}{\partial t} = P_r R_a \nabla T \times \boldsymbol{r} + \nabla \times (\boldsymbol{u} \times \boldsymbol{\omega}) - \nabla \times (\boldsymbol{b} \times \boldsymbol{j}) + P_r T_a^{\frac{1}{2}} \hat{\boldsymbol{z}} \cdot \nabla \boldsymbol{u} + P_r \nabla^2 \boldsymbol{\omega}. \tag{15}$$

The second term on the right-hand side of this equation represents the vortex stretching and tilting (cf. the first term in eq. (2)). Multiplying eq. (15) by $\boldsymbol{\omega}$, and integrating over the spherical shell, we obtain the enstrophy equation

$$\begin{aligned} \frac{d}{dt} \int_{shell} \tfrac{1}{2} |\boldsymbol{\omega}|^2 d\boldsymbol{x} = {} & P_r R_a \int_{shell} \boldsymbol{\omega} \cdot (\nabla T \times \boldsymbol{r})\, d\boldsymbol{x} + \int_{shell} \boldsymbol{\omega} \cdot \underline{\boldsymbol{s}} \cdot \boldsymbol{\omega}\, d\boldsymbol{x} \\ & - \int_{shell} \boldsymbol{b} \cdot (\nabla \boldsymbol{j}) \cdot \boldsymbol{\omega}\, d\boldsymbol{x} + \int_{shell} \boldsymbol{j} \cdot (\nabla \boldsymbol{b}) \cdot \boldsymbol{\omega}\, d\boldsymbol{x} \\ & + P_r T_a^{\frac{1}{2}} \int_{shell} \hat{\boldsymbol{z}} \cdot \underline{\boldsymbol{s}} \cdot \boldsymbol{\omega}\, d\boldsymbol{x} + P_r \int_{shell} \boldsymbol{\omega} \cdot \left(\nabla^2 \boldsymbol{\omega}\right) d\boldsymbol{x}. \end{aligned} \tag{16}$$

The second term on the right-hand side of this equation represents the contribution due to vorticity stretching. In the present case, the mean stretching rate of magnetic flux lines ($\int_{shell} \boldsymbol{b} \cdot \underline{\boldsymbol{s}} \cdot \boldsymbol{b}\, d\boldsymbol{x} / \int_{shell} |\boldsymbol{b}|^2 d\boldsymbol{x} = 7.3$) is much larger than that of vorticity lines ($\int_{shell} \boldsymbol{\omega} \cdot \underline{\boldsymbol{s}} \cdot \boldsymbol{\omega}\, d\boldsymbol{x} / \int_{shell} |\boldsymbol{\omega}|^2 d\boldsymbol{x} = 1.3$). That is, the magnetic flux lines are being stretched more than the vorticity lines. On the other hand, the mean stretching rate of fluid elements, $\int_{shell} \boldsymbol{u} \cdot \underline{\boldsymbol{s}} \cdot \boldsymbol{u}\, d\boldsymbol{x} / \int_{shell} |\boldsymbol{u}|^2 d\boldsymbol{x}$, vanishes exactly because the velocity field is solenoidal and boundary condition is no-slip.

The structure of magnetic field obtained here has some similarities to the observation of the real geomagnetic field.[11] The pattern of magnetic field at the core-mantle boundary is anti-symmetric with respect to the equatorial plane. There is strong magnetic flux in the middle latitude at two of three locations distributed symmetrically around the rotation axis. They drift westward relative to the Earth. These characteristic features of the geomagnetic field are quite similar to those observed in the present simulation though the strong magnetic field is concentrated at two of five symmetric locations instead of three.

A similarity to the sunspots[12] is also to be noted. A sunspot is a sheaf of magnetic flux lines standing in the photosphere, filling the umbra and peumbra, and fanning out above. The magnetic field is strongest and almost radial at the center of the umbra. It gradually weakens with distance from the center. A sunspot is cooler than the surroundings. These features are consistent qualitatively with the present numerical magnetic field.

The structure of intense magnetic field observed in the present simulation rather robust. In fact we have seen that it survives at such a low Roberts number as $R_o = 0.1$ in which the magnetic energy is about 30% of the kinetic and the velocity field changes significantly in time.[8] As a matter of course, the coupling between the velocity and the magnetic fields gets stronger and their spatio-temporal structures may deviate from the present basic structure at further low Roberts numbers. In our preliminary simulation at $R_o = 0.07$, in which irregular reversals of magnetic dipole moment are taking place, the intense magnetic field changes in a quite complicated way but still retains a trace of the basic structure. These results will be reported in a separate paper.

ACKNOWLEDGMENTS

We would like to express our hearty gratitude to Dr. K. Araki for his invaluable comments and for his help in an improvement of the numerical code. This work was partially supported by a Grant-in-Aid for Scientific Research from the Ministry of Education, Science and Culture of Japan.

REFERENCES

[1] E. N. Parker, "Hydromagnetic dynamo models." Astrophys. J. **122**, 293 (1955).

[2] P. H. Roberts and A. M. Soward, "Dynamo theory." Annu. Rev. Fluid Mech. **24**, 459 (1992).

[3] P. H. Roberts, "Kinematic dynamo models." Phil. Trans. R. Soc. London Ser. A **272**, 663 (1972).

[4] A. Kageyama, T. Sato, and the Complexity Simulation Group, "Computer simulation of a magnetohydrodynamic dynamo. II," Phys. Plasmas **2**, 1421 (1995).

[5] A. Kageyama and T. Sato, "Velocity and magnetic field structures in a magnetohydrodynamic dynamo," Phys. Plasmas **4**, 1569 (1997).

[6] A. Kageyama and T. Sato, "Generation mechanism of a dipole field by a magnetohydrodynamic dynamo," Phys. Rev. E **55**, 4617 (1997).

[7] G. A. Glatzmaier and P. H. Roberts, "A three-dimensional convective dynamo solution with rotating and finitely conducting inner core and mantle," Phys. Earth Planet. Inter. **91**, 63 (1995).

[8] S. Kida, K. Araki, and H. Kitauchi, "Periodic reversals of magnetic field generated by thermal convection in a rotating spherical shell," J. Phys. Soc. Japan **66**, 2194 (1997).

[9] H. Kitauchi, K. Araki, and S. Kida, "Flow structure of thermal convection in a rotating spherical shell," Nonlinearity **10**, 885 (1997).

[10] K. Araki, H. Kitauchi, and S. Kida, Kokyuroku RIMS, **970**, 54 (1996) (in Japanese).

[11] D. Gubbins and J. Bloxham, "Morphology of the geomagnetic field and implications for the geodynamo," Nature **325**, 509 (1987).

[12] R. Moore and D. Rabin, "Sunspots," Ann. Rev. Astron. Astrophys. **23**, 239 (1985).

FIGURE CAPTIONS

FIG. 1. Configuration of the system.

FIG. 2. (a) Temporal evolution of kinetic energy $\mathcal{E}_K$ and total magnetic energy $\mathcal{E}_M$. The total magnetic energy in the quasi-steady state is enlarged in (b).

FIG. 3. Temporal evolution of axial component m_z of magnetic dipole moment.

FIG. 4. Iso-surface of magnitude of magnetic flux density $|\boldsymbol{b}| = 2$ ($|\boldsymbol{b}|_{\max} = 3.4$) over two periods of oscillation of $\mathcal{E}_M$ (one period of oscillation of m_z). They are viewed (a) from the north pole and (b) from an oblique angle. Dark (or light) blue implies that the z-component b_z of the magnetic flux density is positive (or negative). Transparent iso-surfaces of vorticity magnitude $|\boldsymbol{\omega}| = 52$ are drawn in region $1.15r_1 \leq r \leq 0.91r_2$. (i) $t = 385$, (ii) 389, (iii) 393, (iv) 397, (v) 401, (vi) 405, (vii) 409, (viii) 413, (ix) 417. (c) Time-evolution of (i) the total magnetic energy and (ii) the axial component of magnetic dipole moment.

FIG. 5. Envelope surface of magnitude of magnetic flux density. The supreme at each point of $|\boldsymbol{b}|$ over time interval $385 \leq t \leq 433$ (three periods of oscillation of $\mathcal{E}_M$) is drawn at the level of $|\boldsymbol{b}| = 2$. They are viewed (a) from the north pole, (b) from an oblique angle and (c) from the equatorial plane.

FIG. 6. Points P1, P2 and P3 of local maximum of magnitude of magnetic flux density in the three kinds of domains of strong magnetic field at $t = 385$.

FIG. 7. (a) Magnetic flux lines which pass a circle of radius 0.15 centered at P1 on a plane perpendicular to $\boldsymbol{b}$. (b) Streamlines projected on a sphere of radius $0.97r_2$. The radial component u_r of velocity is represented by contour lines at the levels of $0, \pm 0.18, \pm 0.36$ and by color map, where dark blue denotes positive and light blue negative. (c) Streamlines which pass a circle of radius 0.2 centered at P1 on a plane perpendicular to the velocity vector. (d) Superposition of the magnetic flux lines in (a) and the

streamlines in (c). (e) A streamline which passes P1, on which P1U and P1D denote the null points of S. (f) Magnetic flux lines which pass the streamline between P1U and P1D. Color in (b), (c) and (f) represents the sign of acceleration a, whereas the sign of stretching term S in (d) and (e); red denotes positive and white negative.

FIG. 8. Variations along the streamline shown in figure 7 (e) of (a) the stretching (S), the advection (A) and the diffusion/dissipation (D) terms and (b) the acceleration a of fluid motion, the angle $\vartheta_{\boldsymbol{b}}$ between the velocity and the magnetic flux vectors and the magnitude of magnetic flux density $|\boldsymbol{b}|$.

FIG. 9. Same as figure 7 around point P2 except for (b), in which streamlines are drawn on the equatorial plane. The rate of strain $\partial u_z/\partial z$ in the axial direction is represented by contour lines at the levels of $0, \pm 6, \pm 12$ and by color map, where dark blue denotes positive and light blue negative.

FIG. 10. Same as figure 8 for a streamline shown in figure 9 (e).

FIG. 11. Same as figure 7 around point P3 except for (b), in which streamlines are drawn on a sphere of radius $1.06r_1$. The radial component u_r of the velocity is represented by contour lines at the levels of $0, \pm 0.5, \pm 1$ and by color map.

FIG. 12. Same as figure 8 for a streamline shown in figure 10 (e).

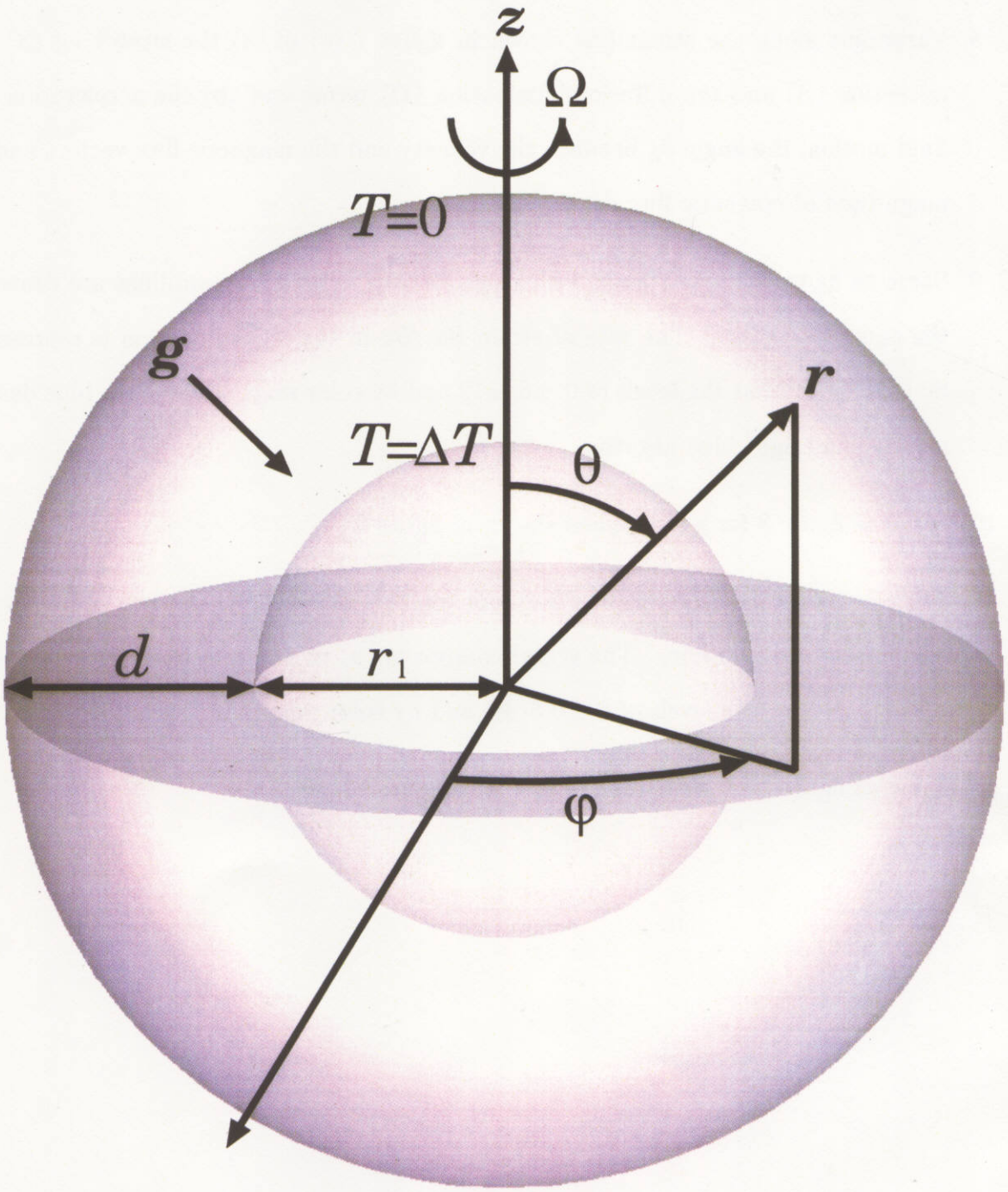

Fig. 1:
H. Kitauchi and S. Kida

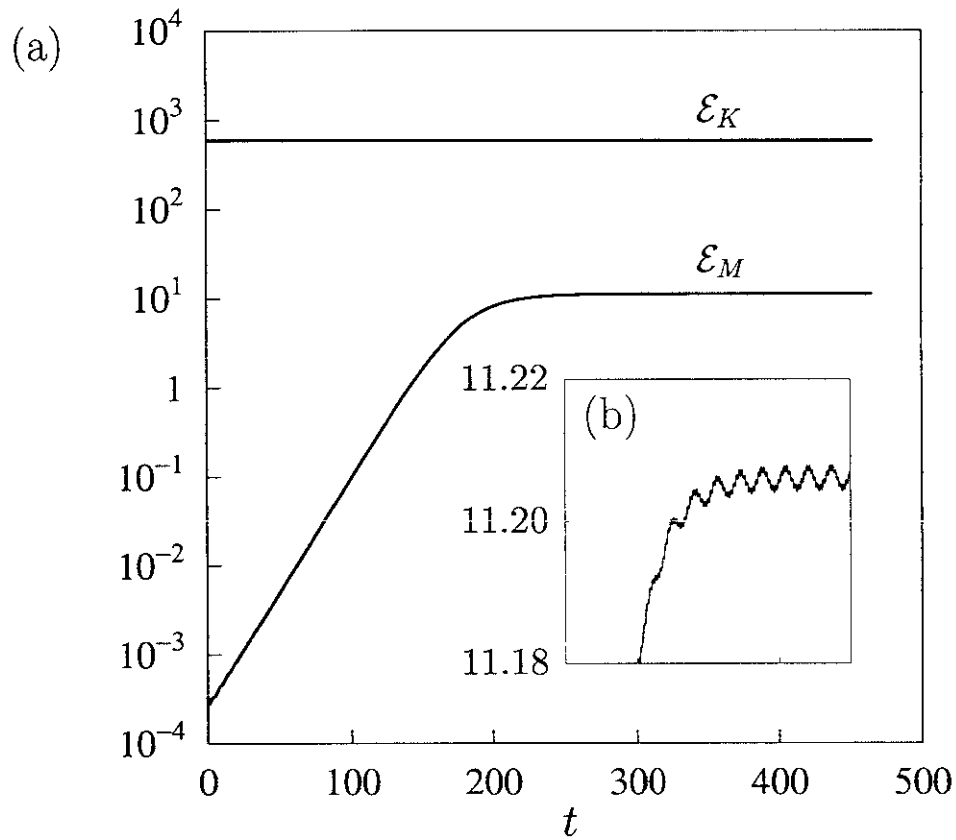

Fig. 2:
H. Kitauchi and S. Kida

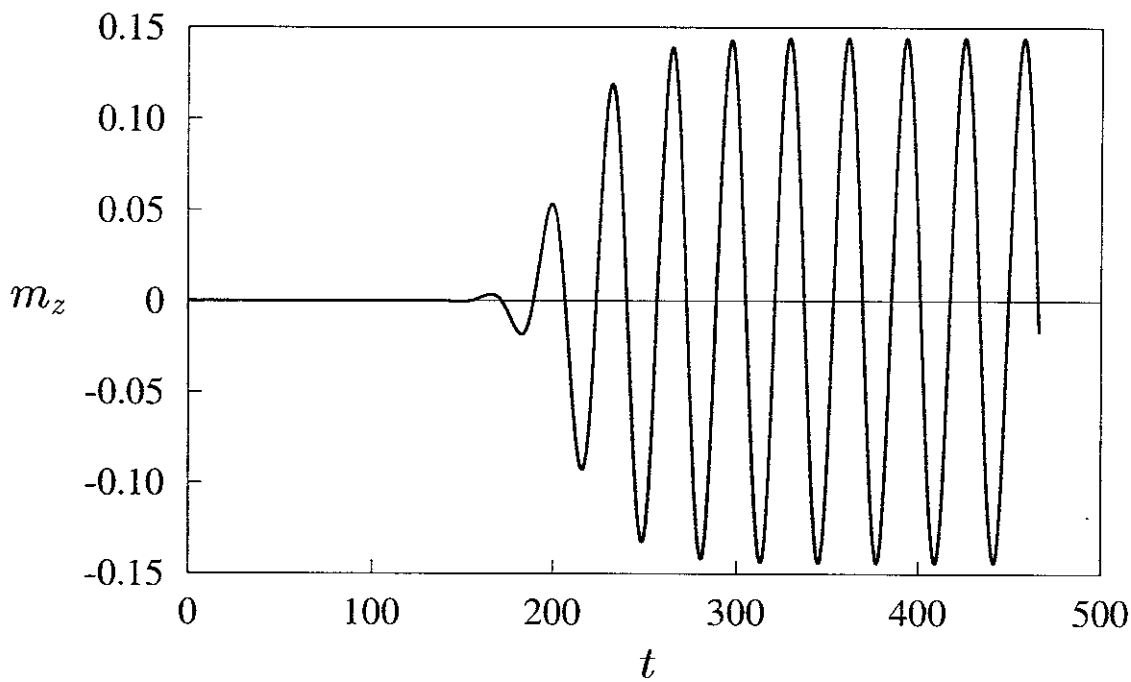

Fig. 3:

H. Kitauchi and S. Kida

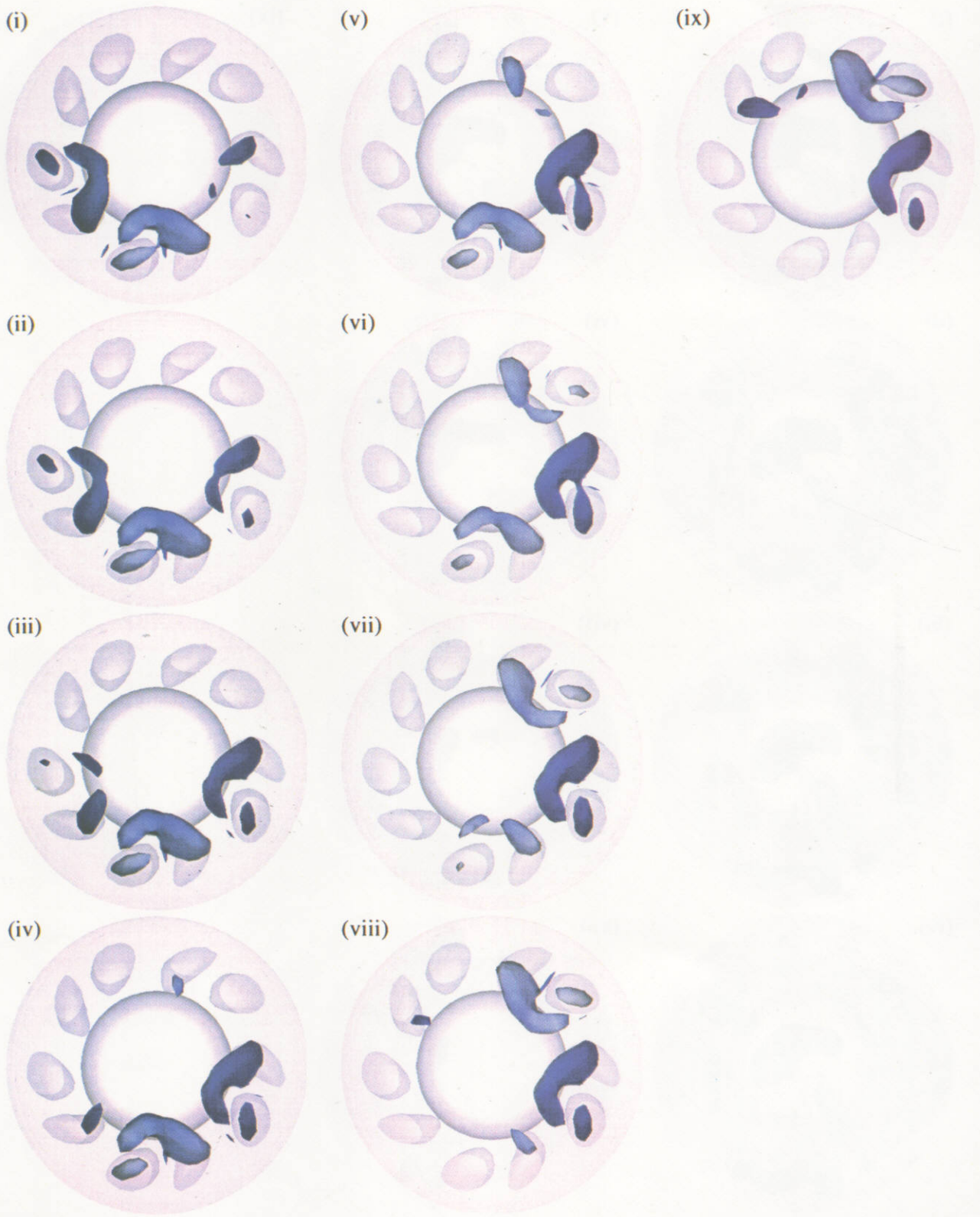

Fig. 4 (a):
H. Kitauchi and S. Kida

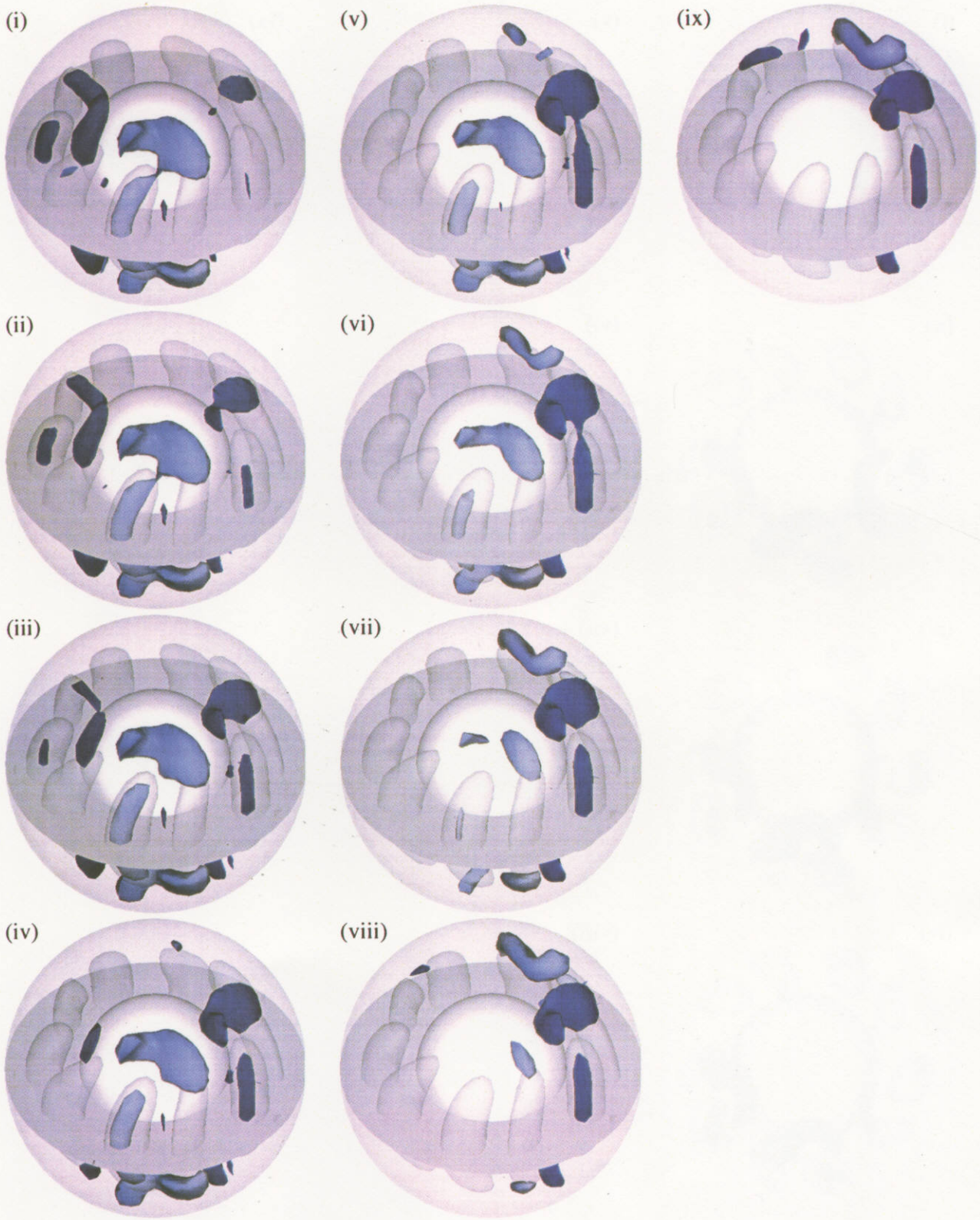

Fig. 4 (b):
H. Kitauchi and S. Kida

(i)

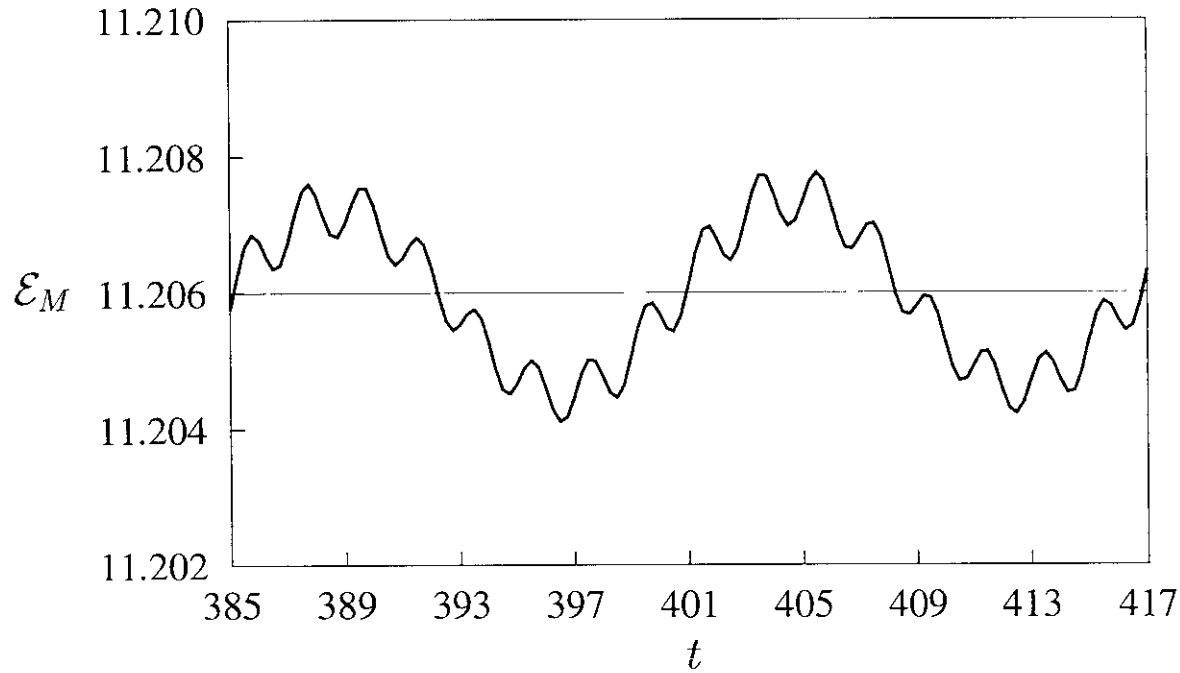

(ii)

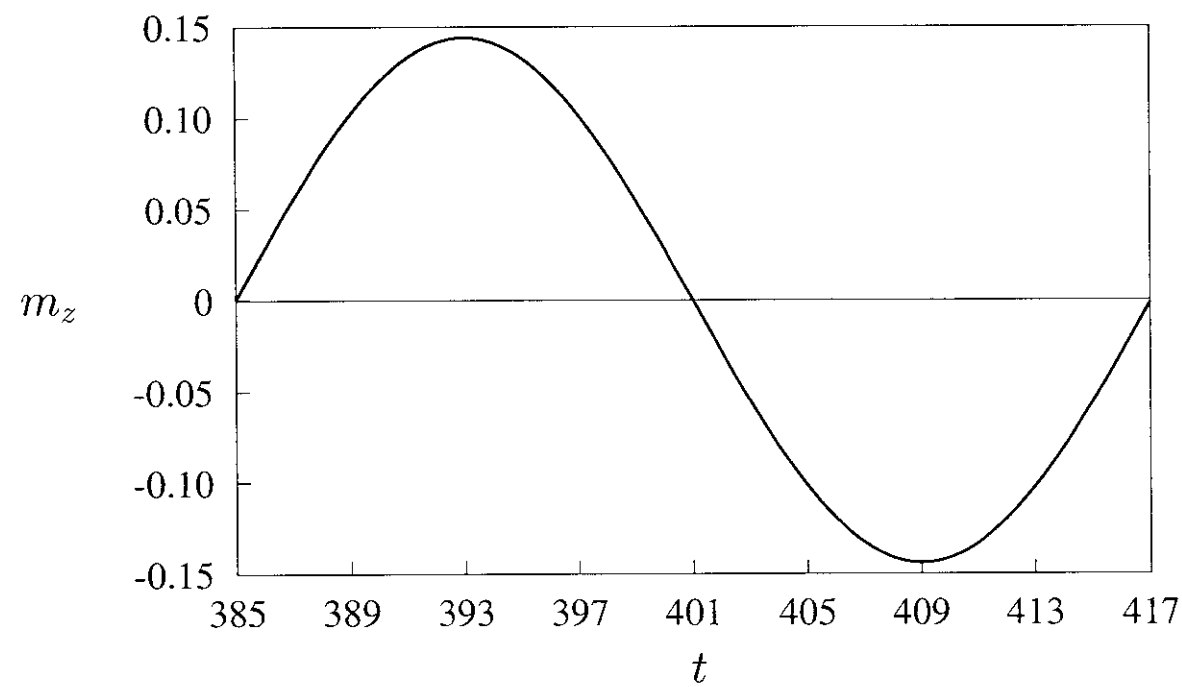

Fig. 4 (c):
H. Kitauchi and S. Kida

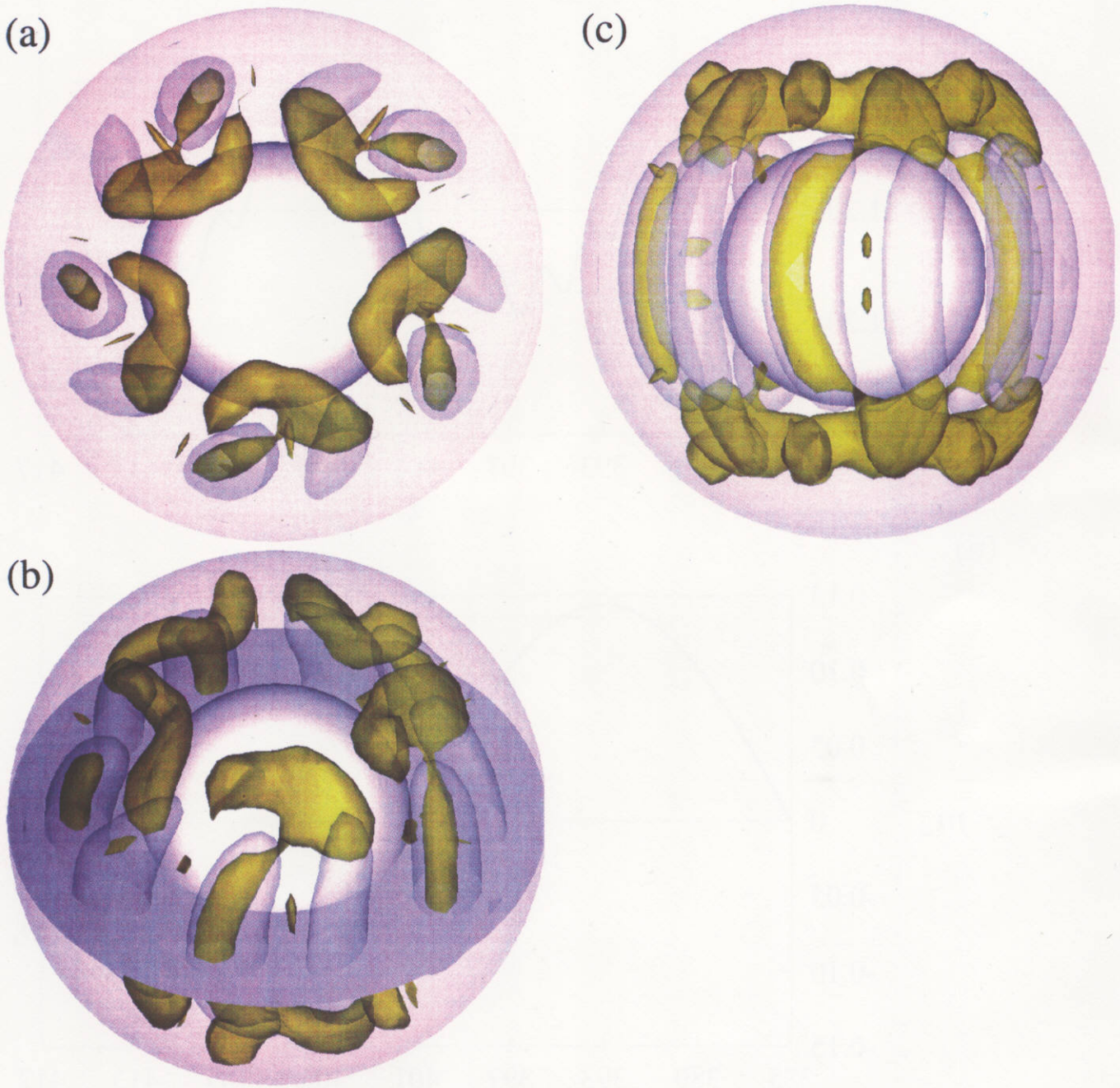

Fig. 5:
H. Kitauchi and S. Kida

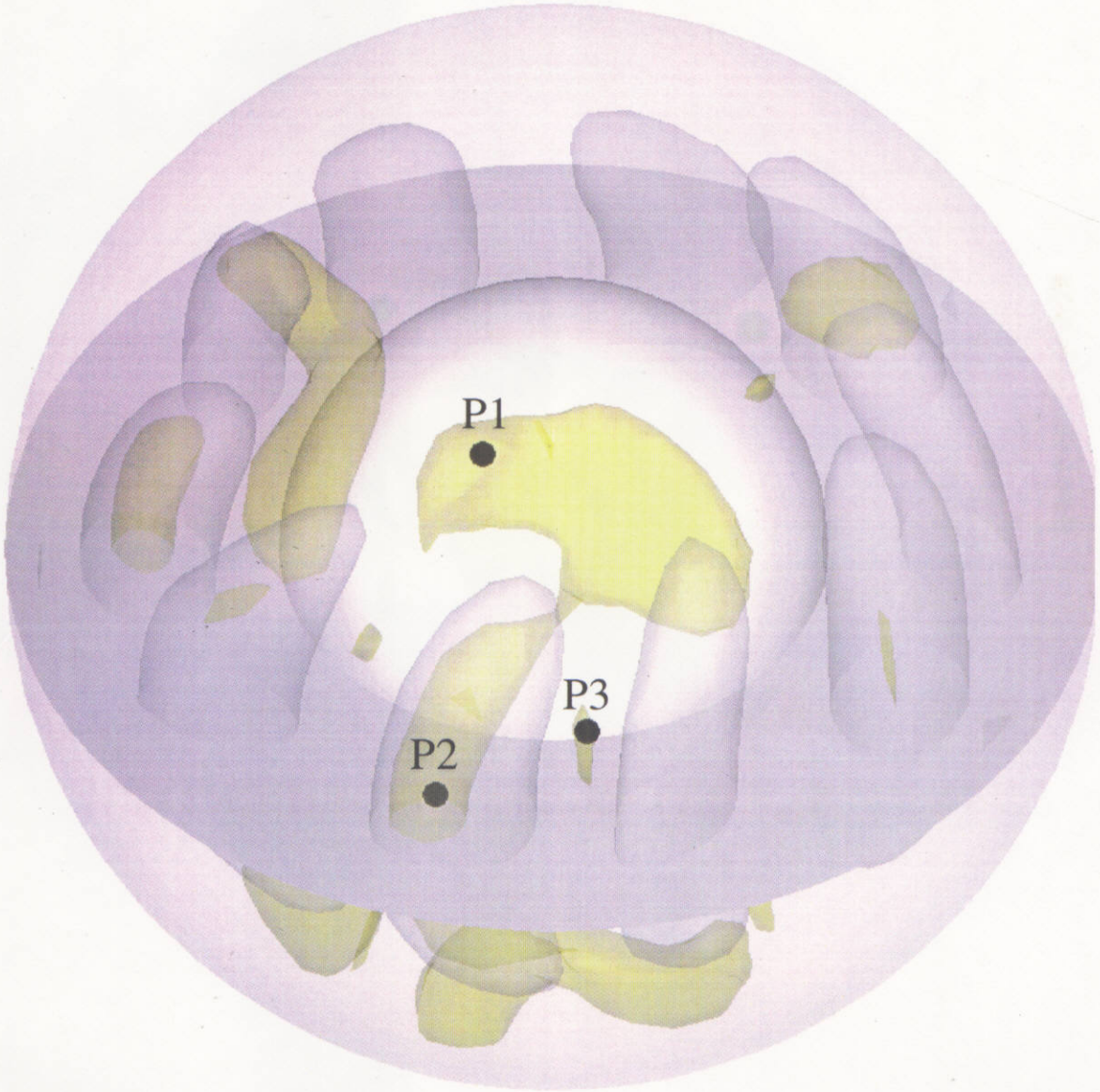

Fig. 6:
H. Kitauchi and S. Kida

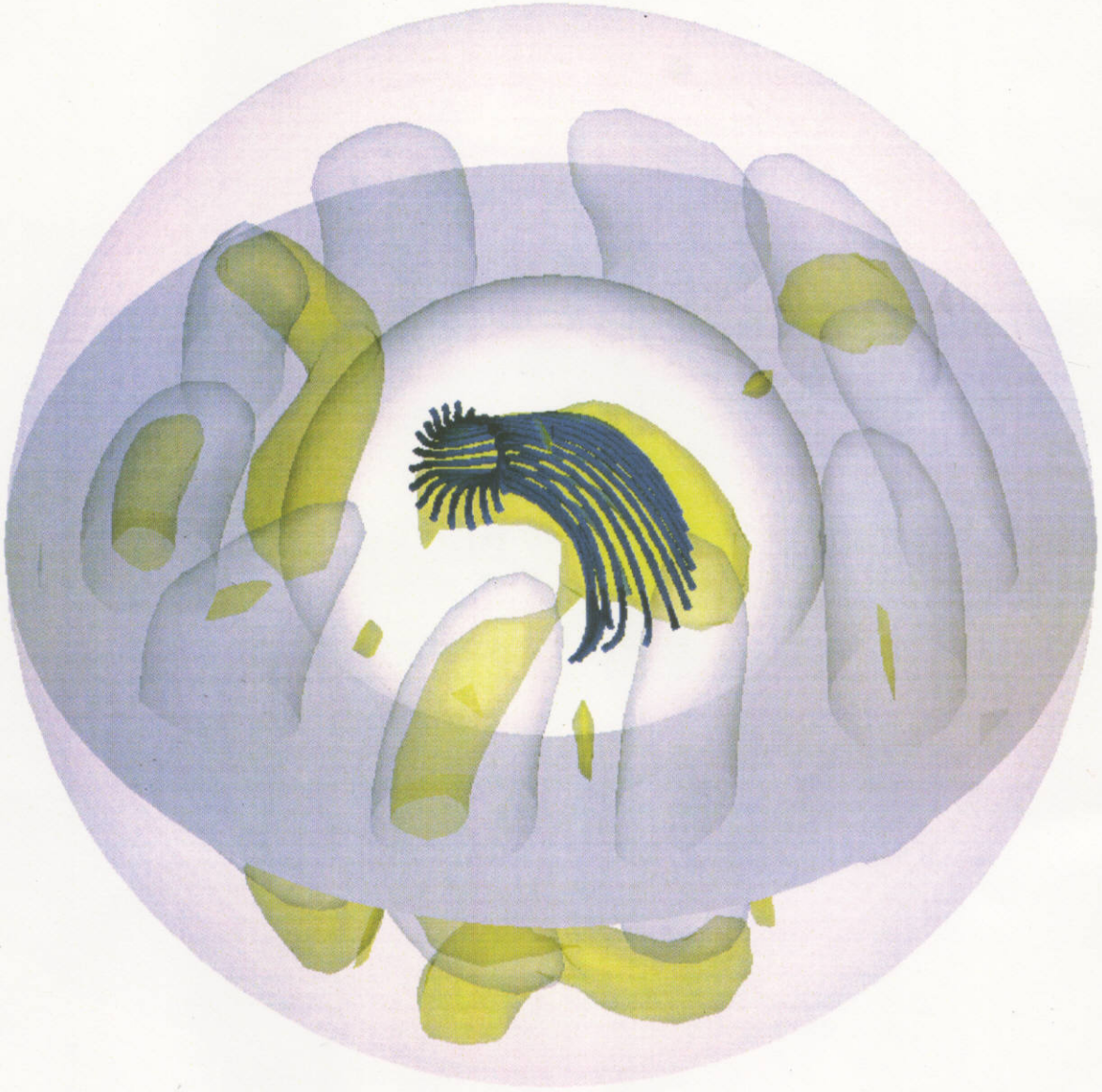

Fig. 7 (a):
H. Kitauchi and S. Kida

Fig. 7 (b):
H. Kitauchi and S. Kida

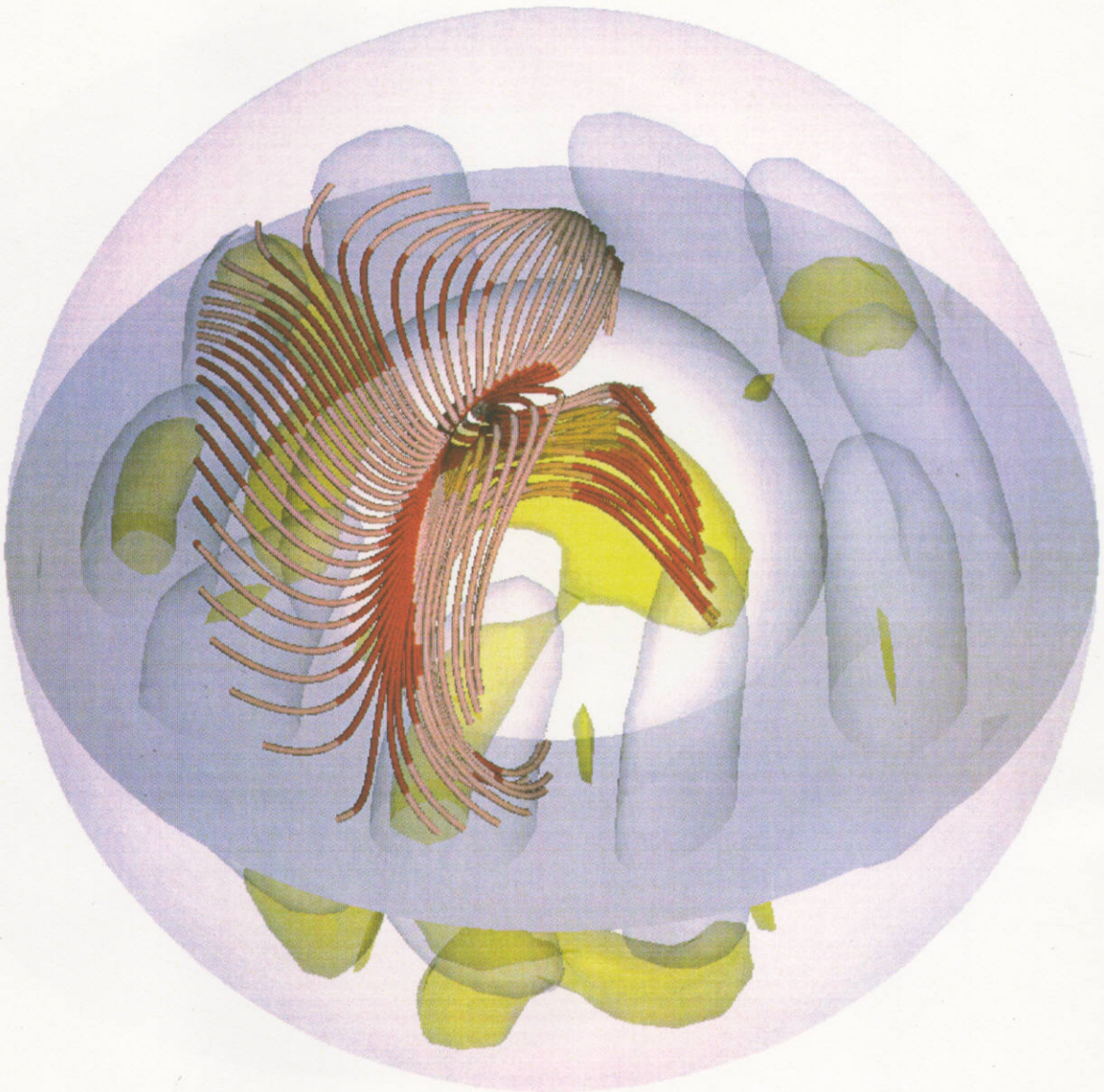

Fig. 7 (c):
H. Kitauchi and S. Kida

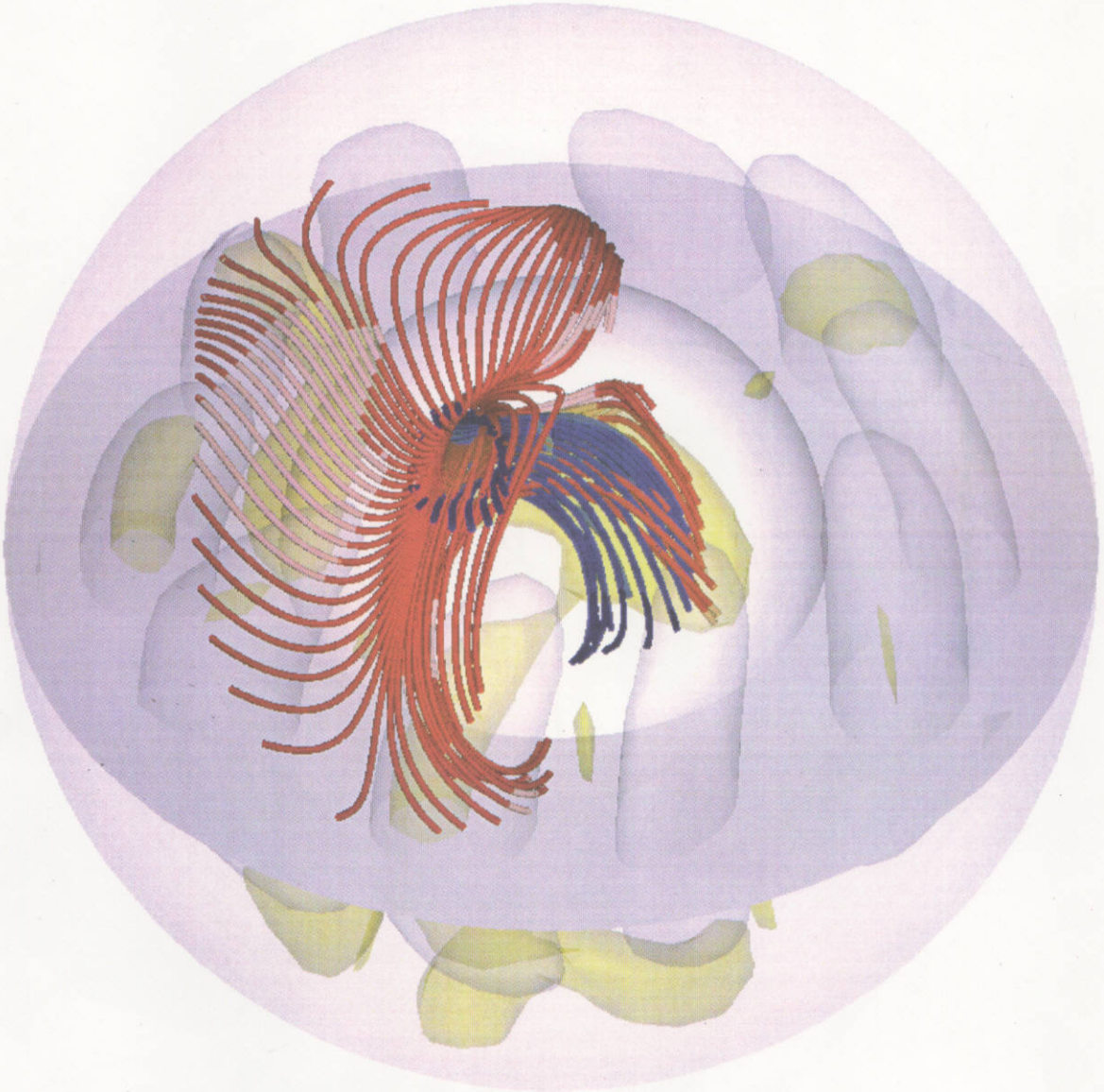

Fig. 7 (d):
H. Kitauchi and S. Kida

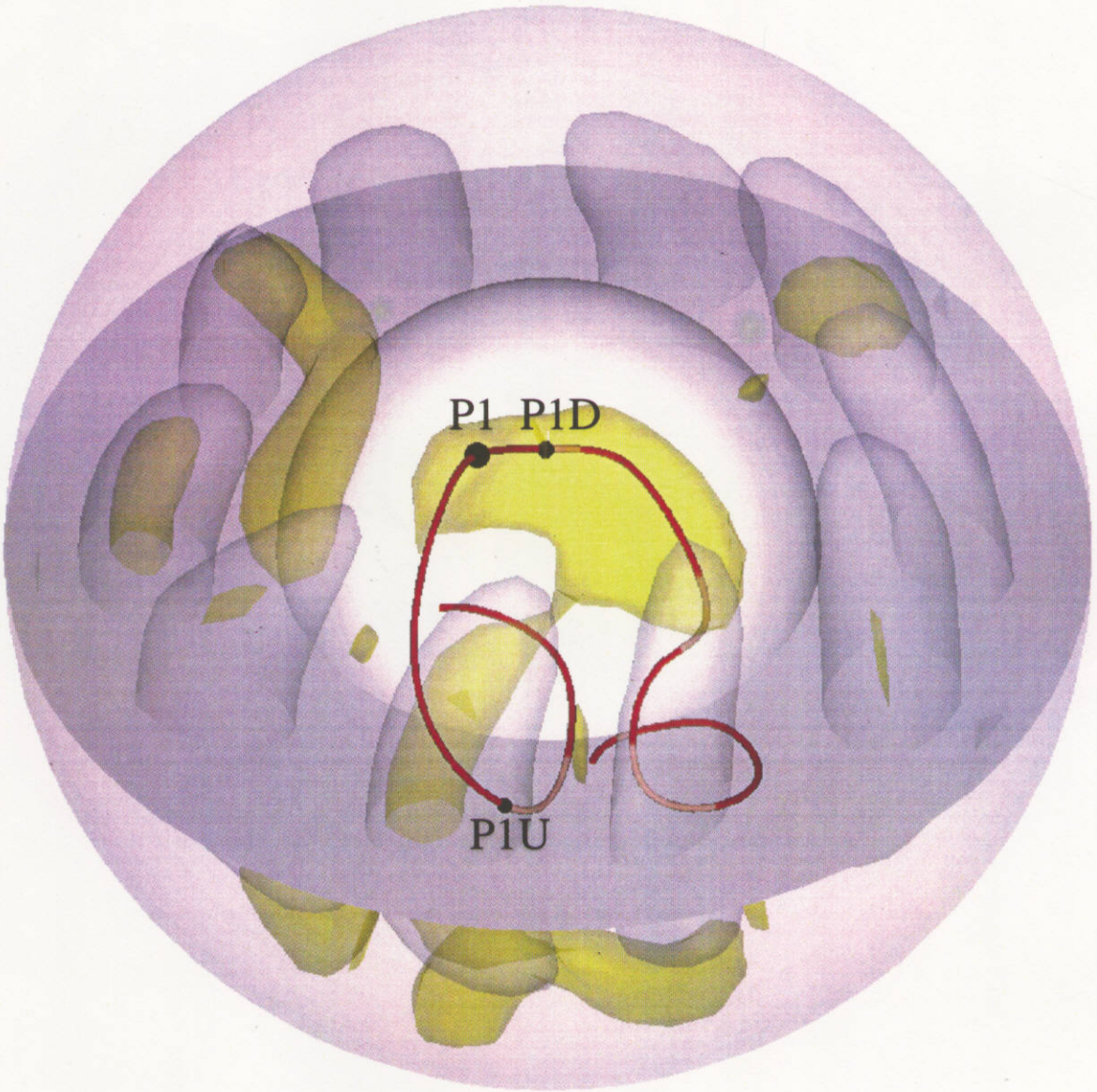

Fig. 7 (e):
H. Kitauchi and S. Kida

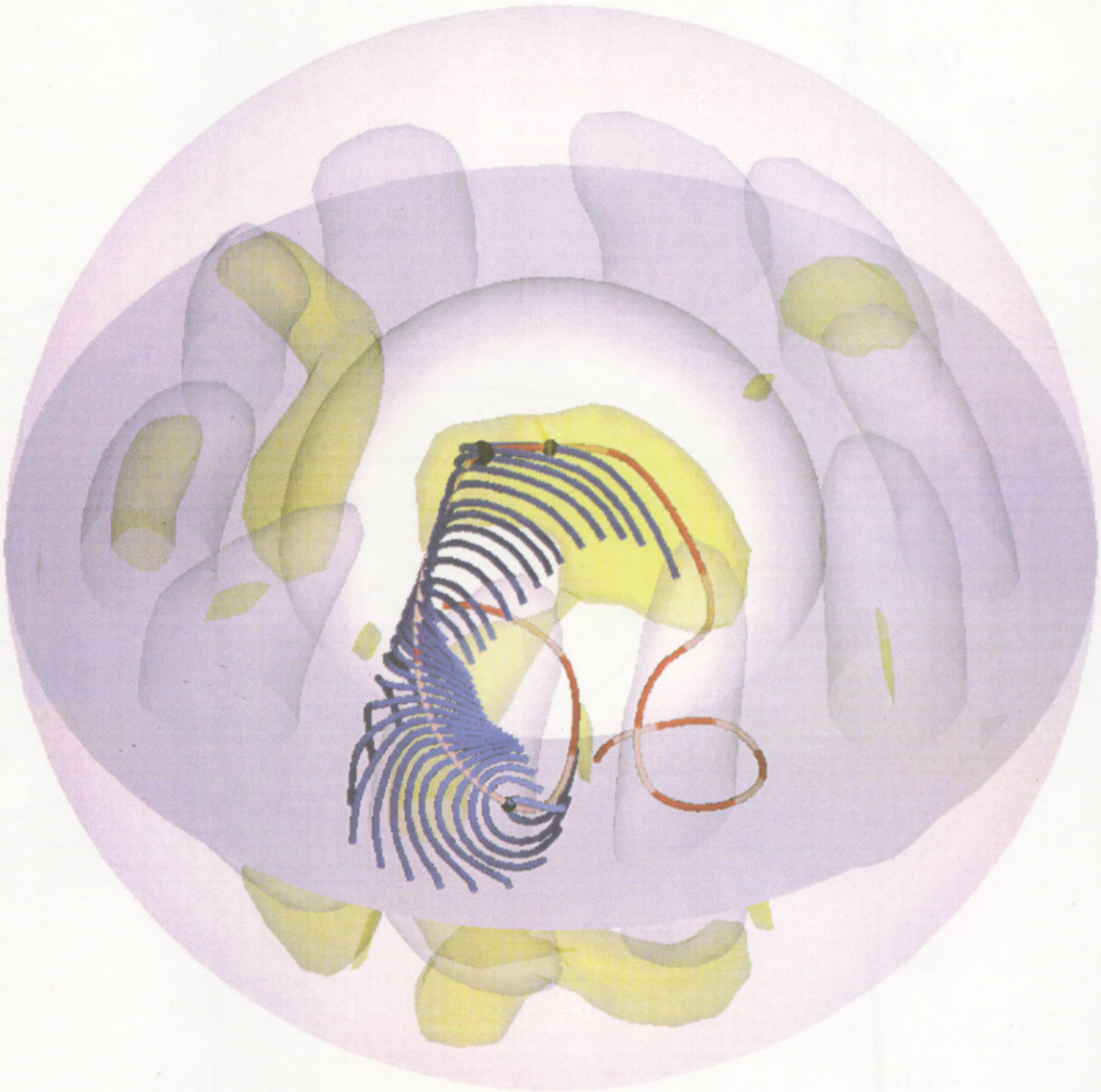

Fig. 7 (f):
H. Kitauchi and S. Kida

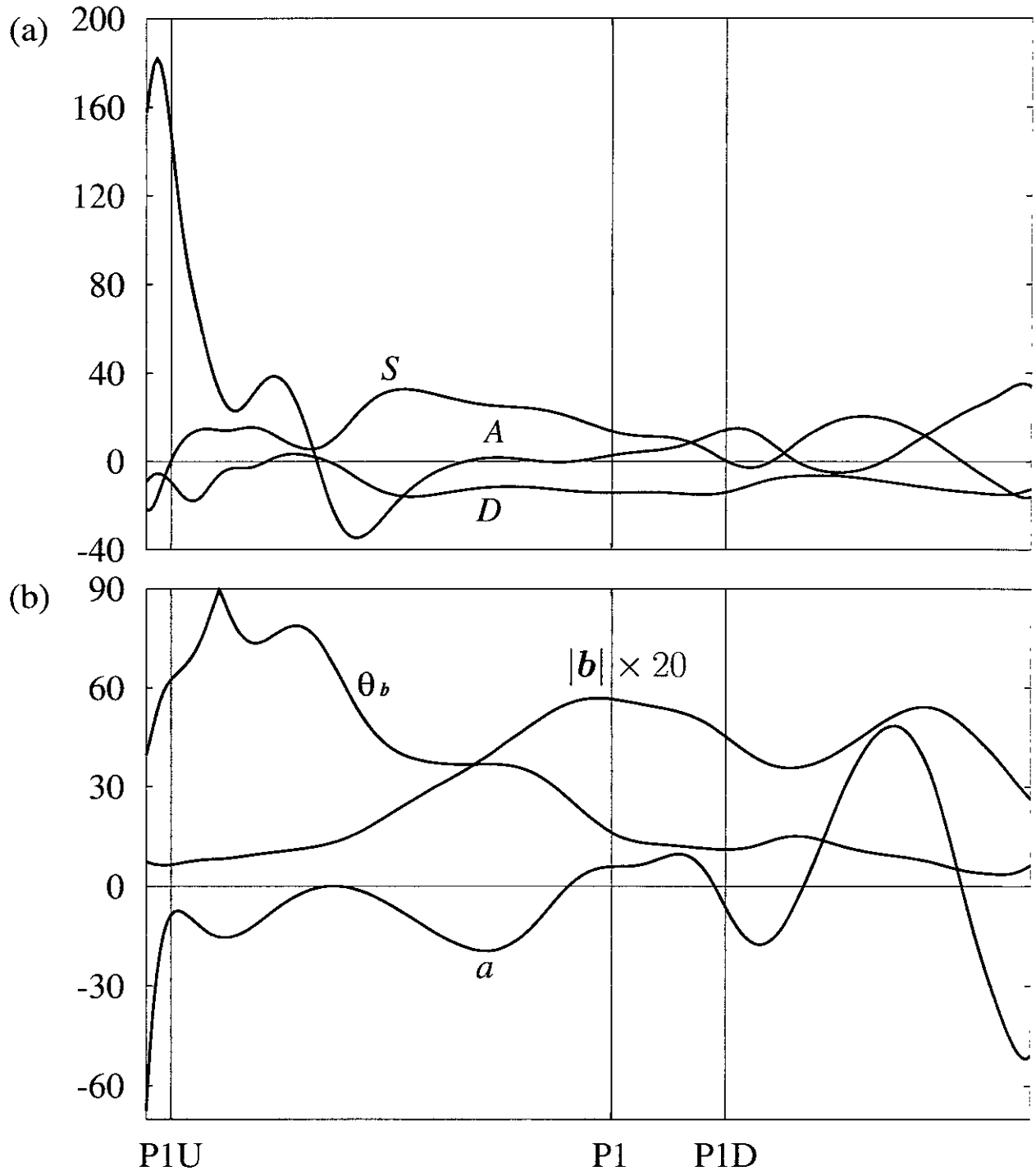

Fig. 8:
H. Kitauchi and S. Kida

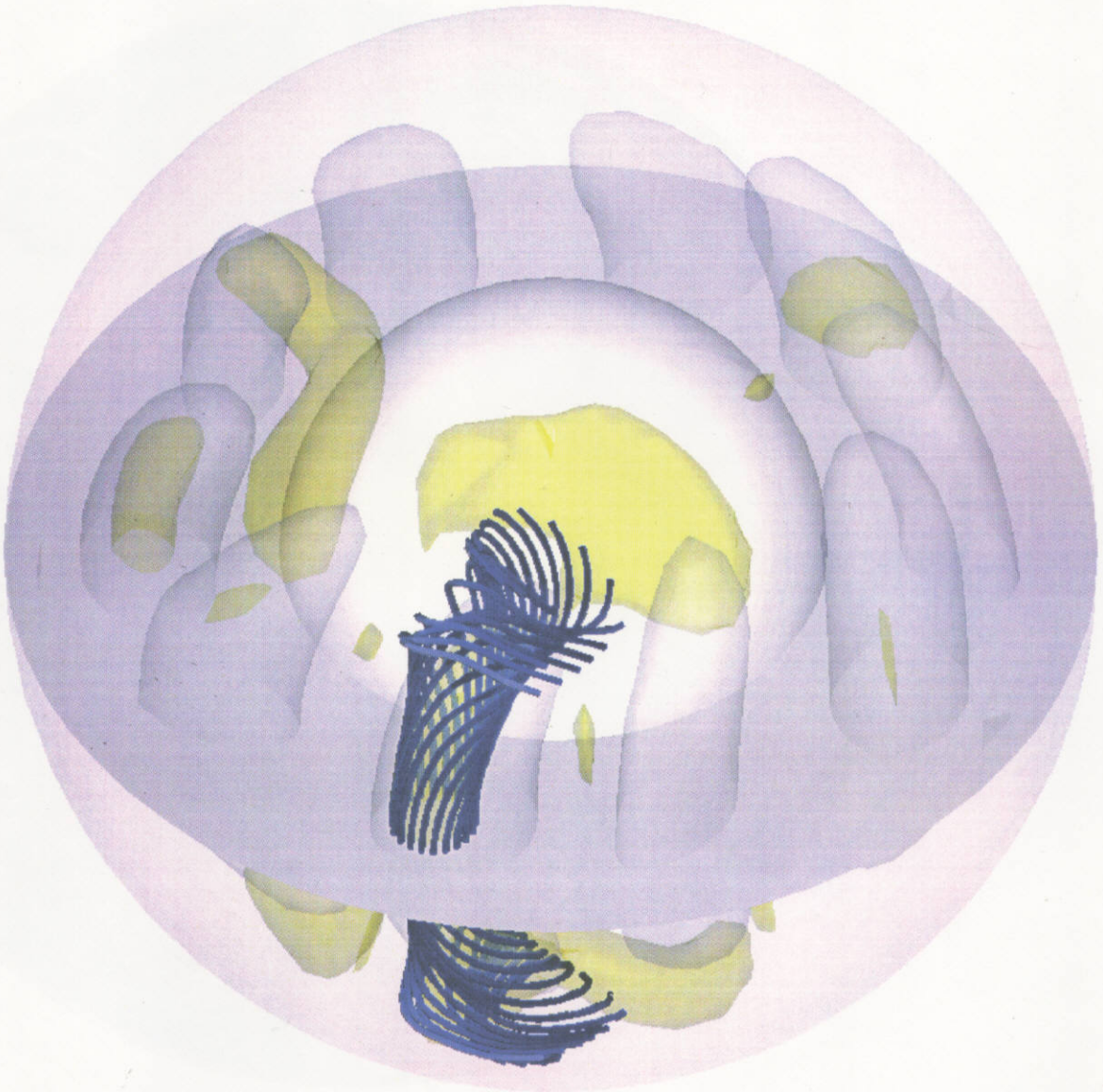

Fig. 9 (a):
H. Kitauchi and S. Kida

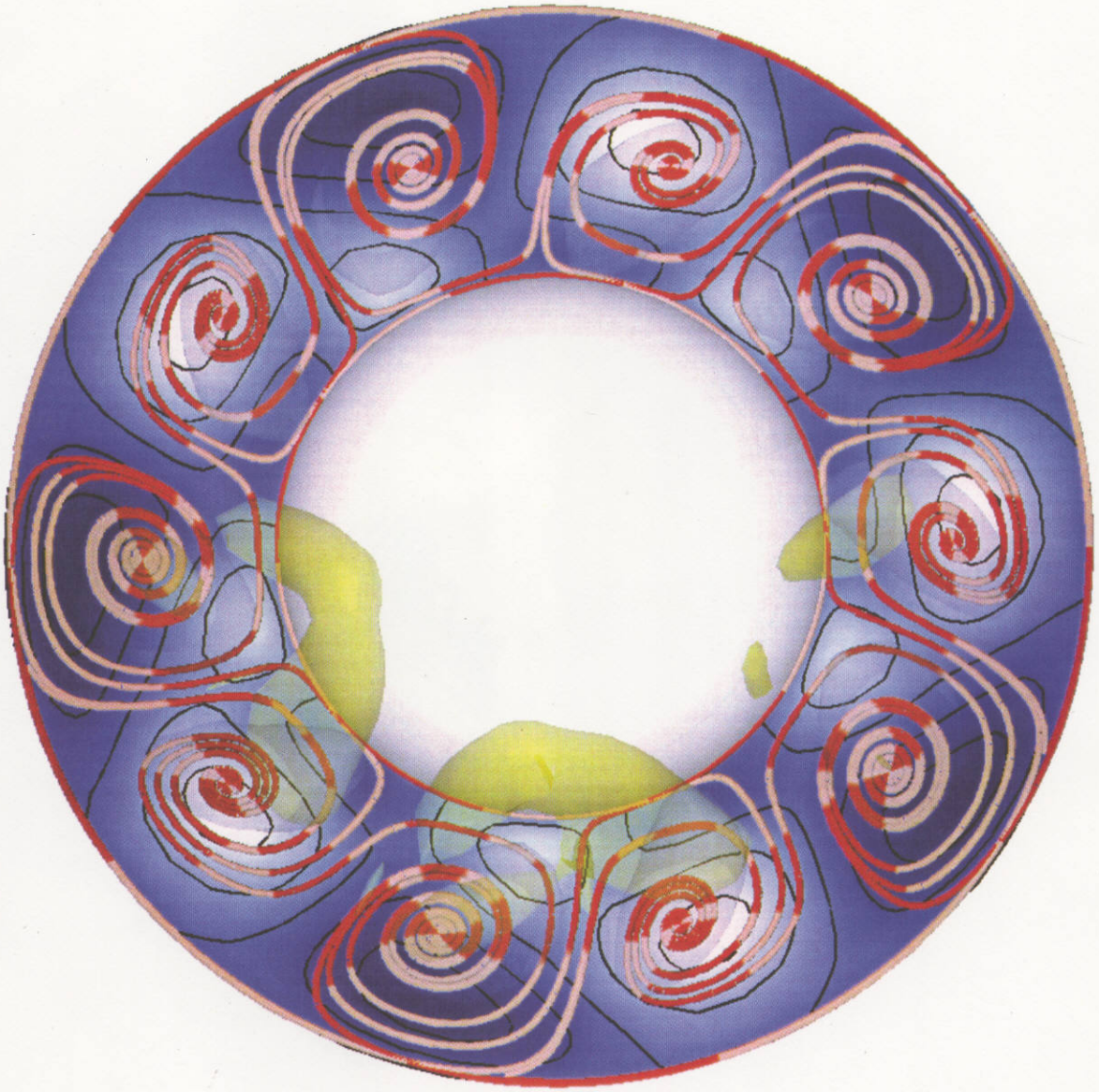

Fig. 9 (b):
H. Kitauchi and S. Kida

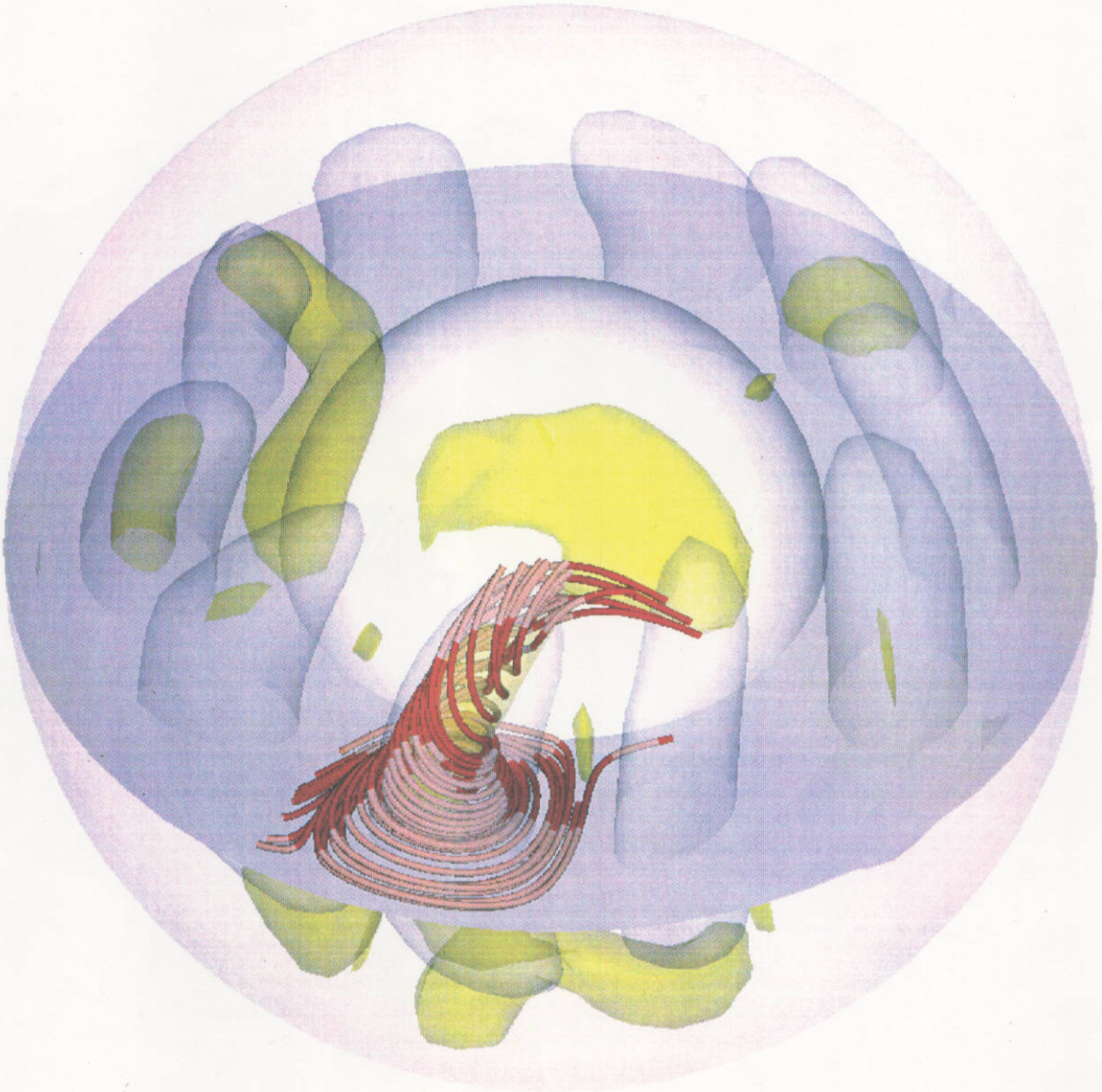

Fig. 9 (c):
H. Kitauchi and S. Kida

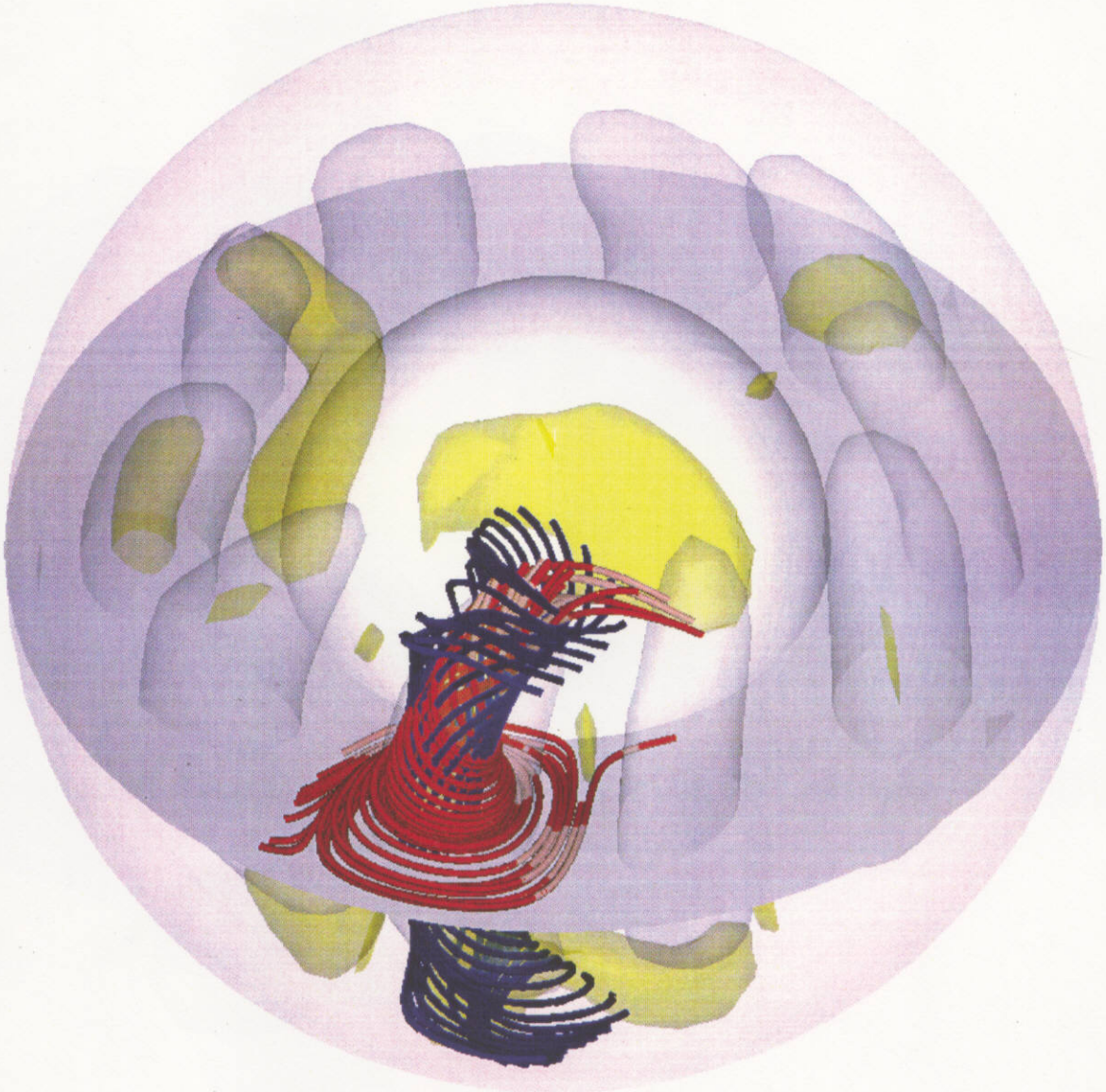

Fig. 9 (d):
H. Kitauchi and S. Kida

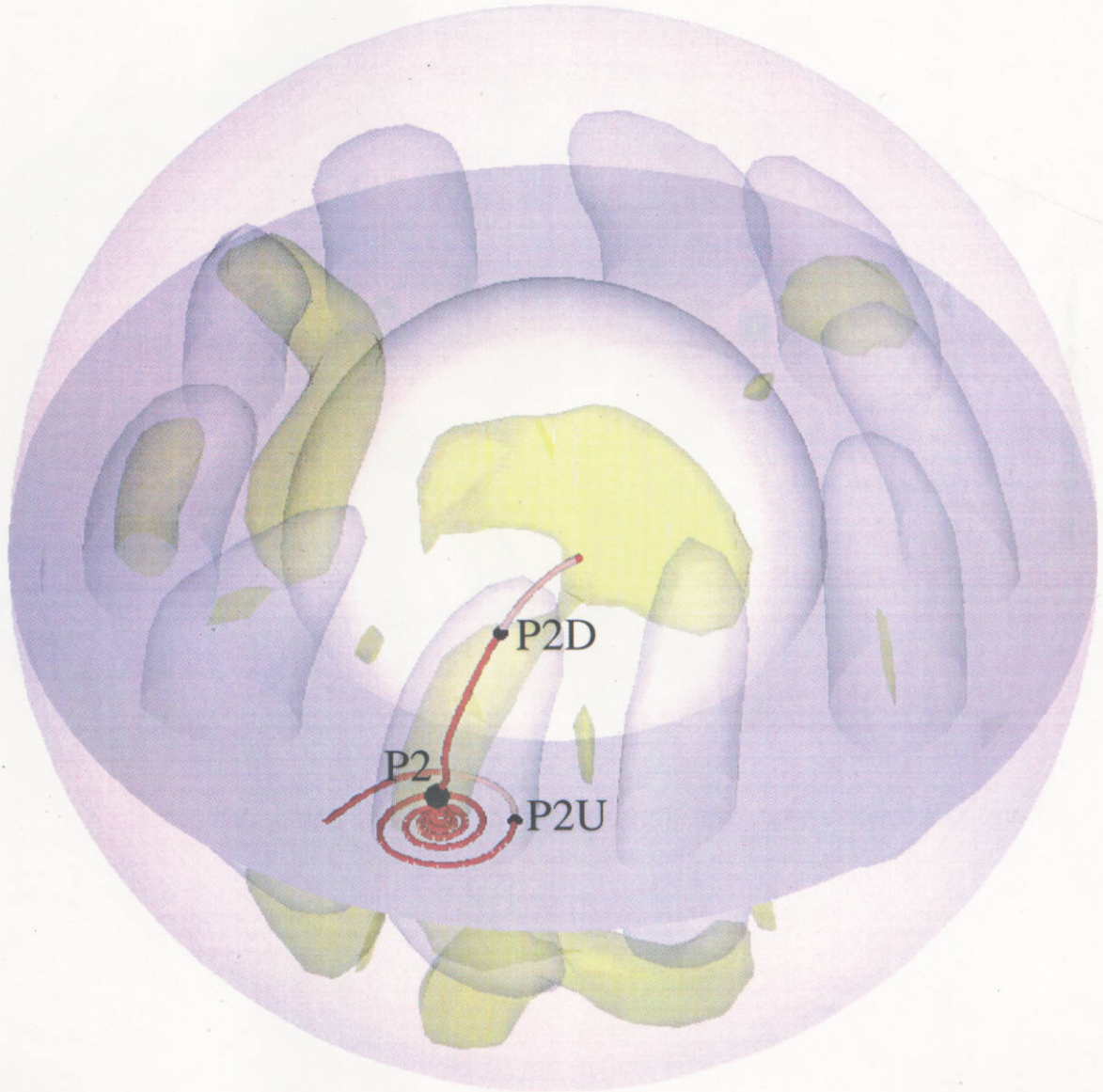

Fig. 9 (e):
H. Kitauchi and S. Kida

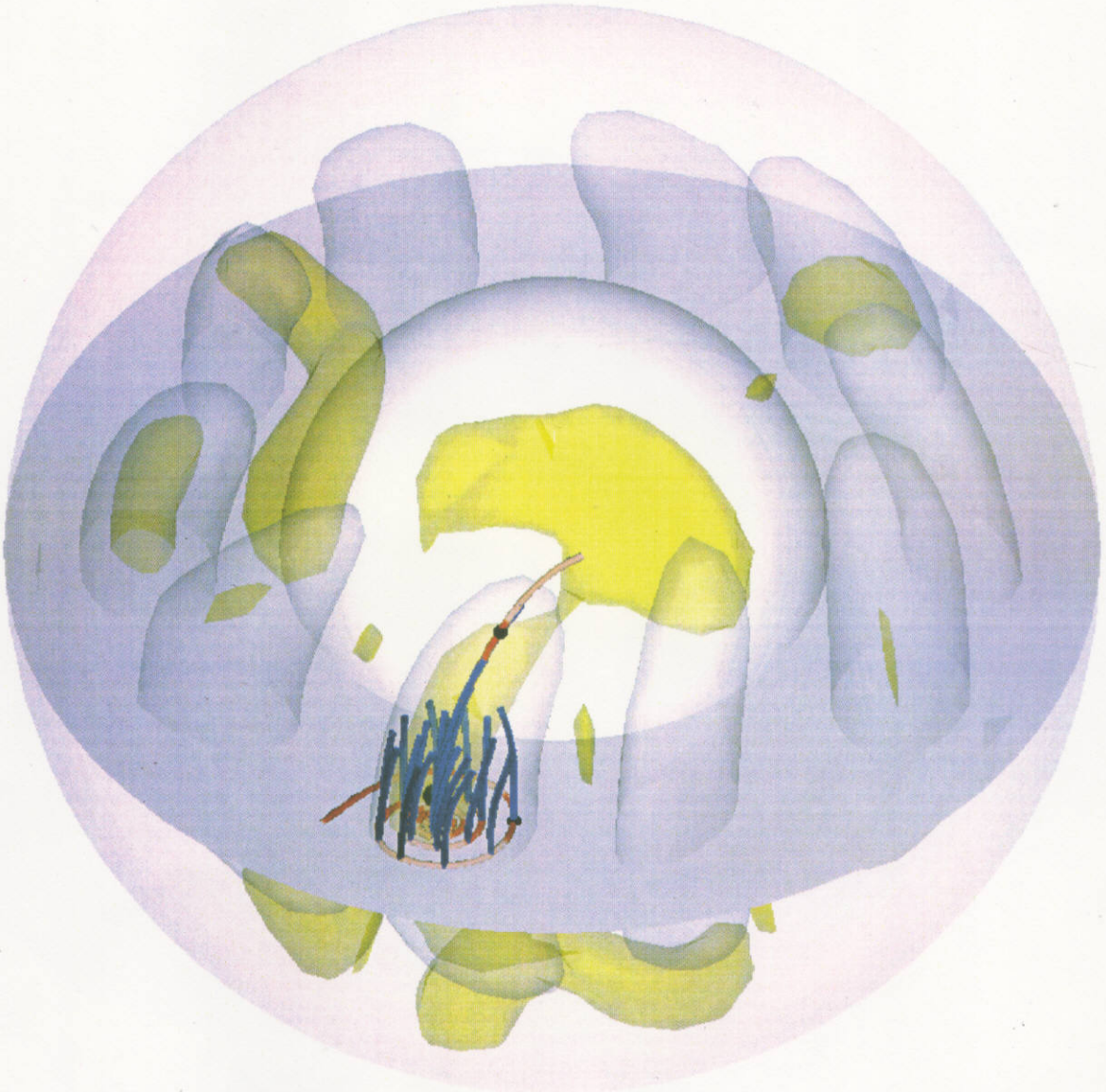

Fig. 9 (f):
H. Kitauchi and S. Kida

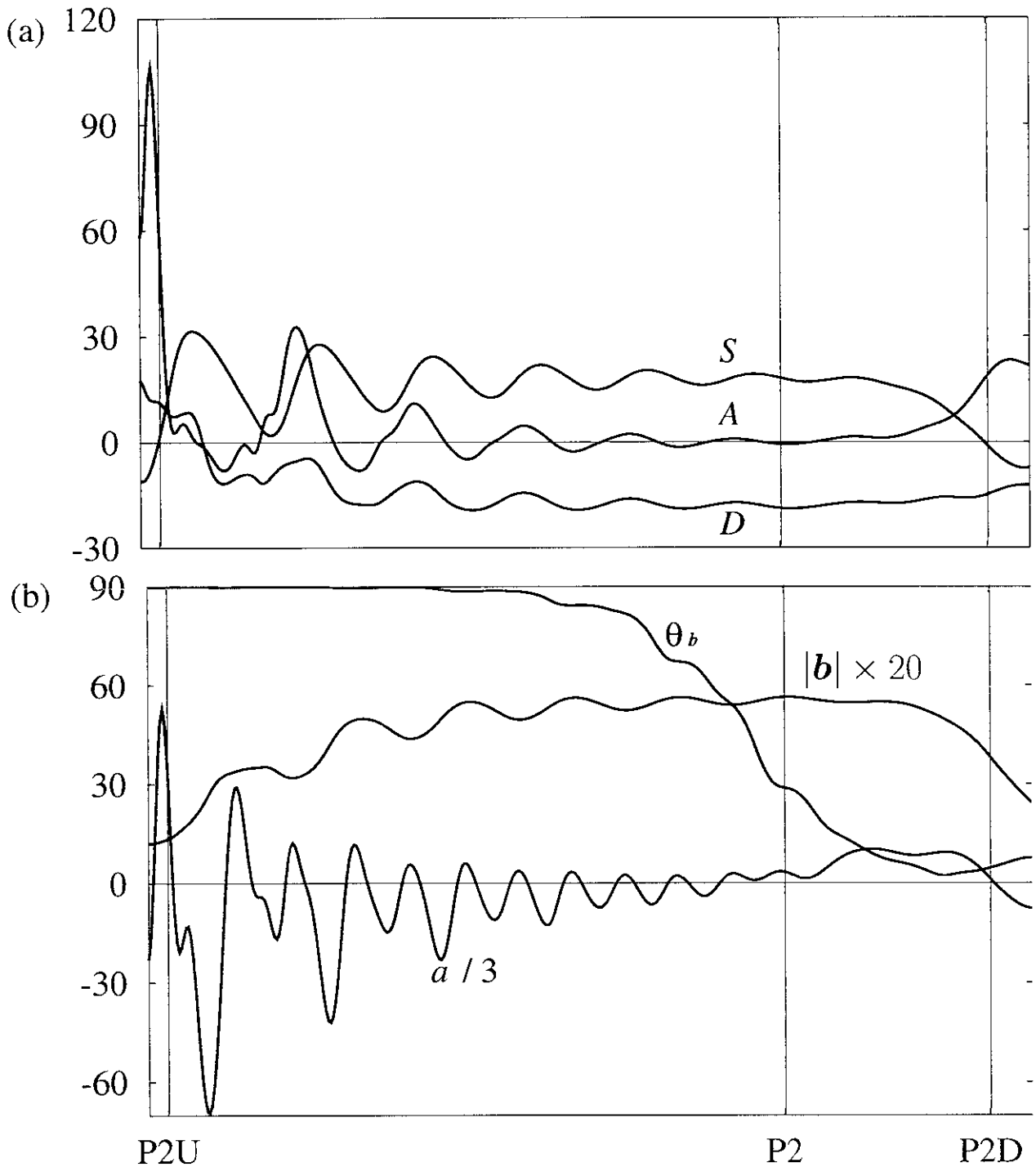

Fig. 10:
H. Kitauchi and S. Kida

Fig. 11 (a):
H. Kitauchi and S. Kida

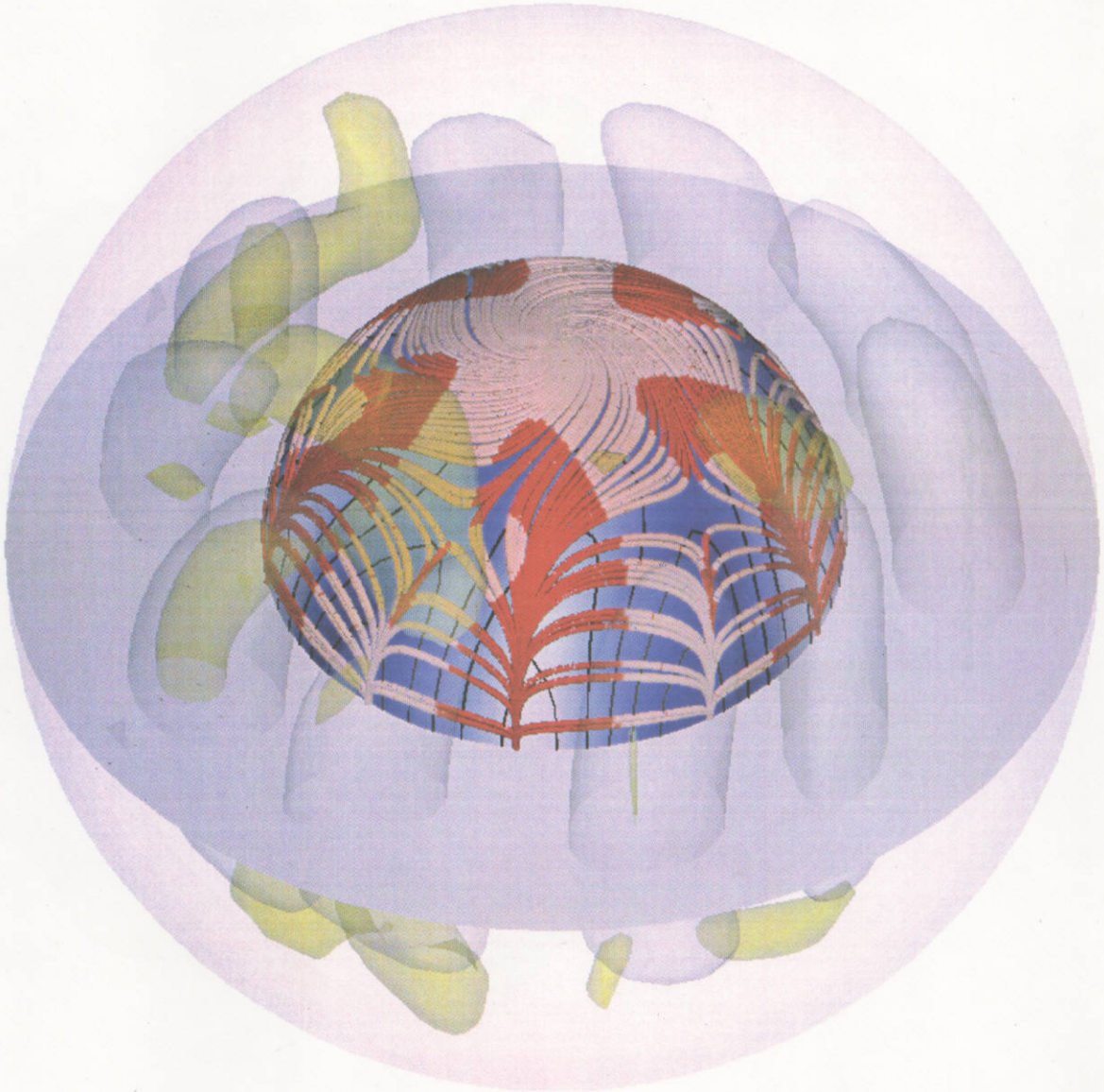

Fig. 11 (b):
H. Kitauchi and S. Kida

Fig. 11 (c):
H. Kitauchi and S. Kida

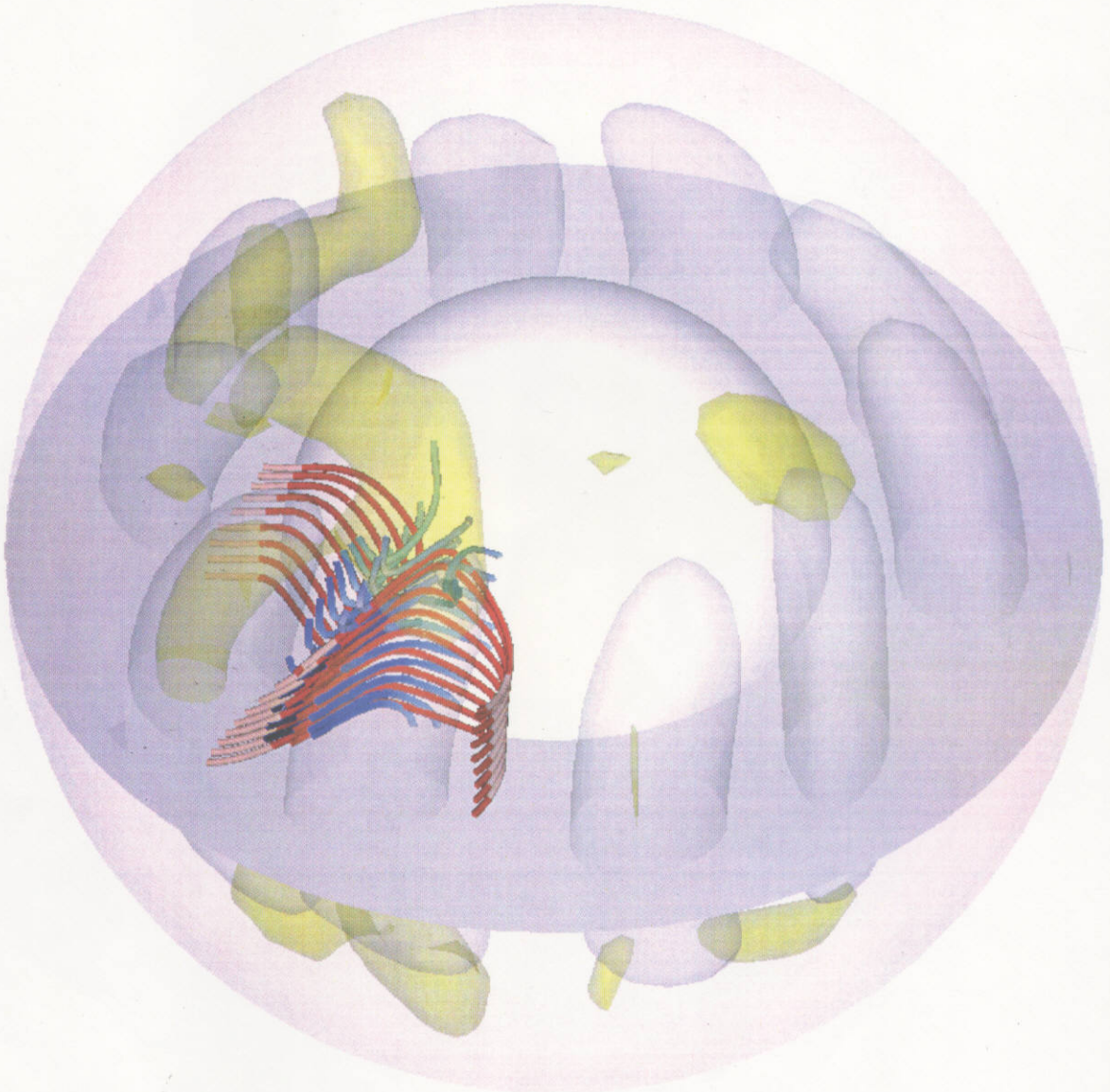

Fig. 11 (d):
H. Kitauchi and S. Kida

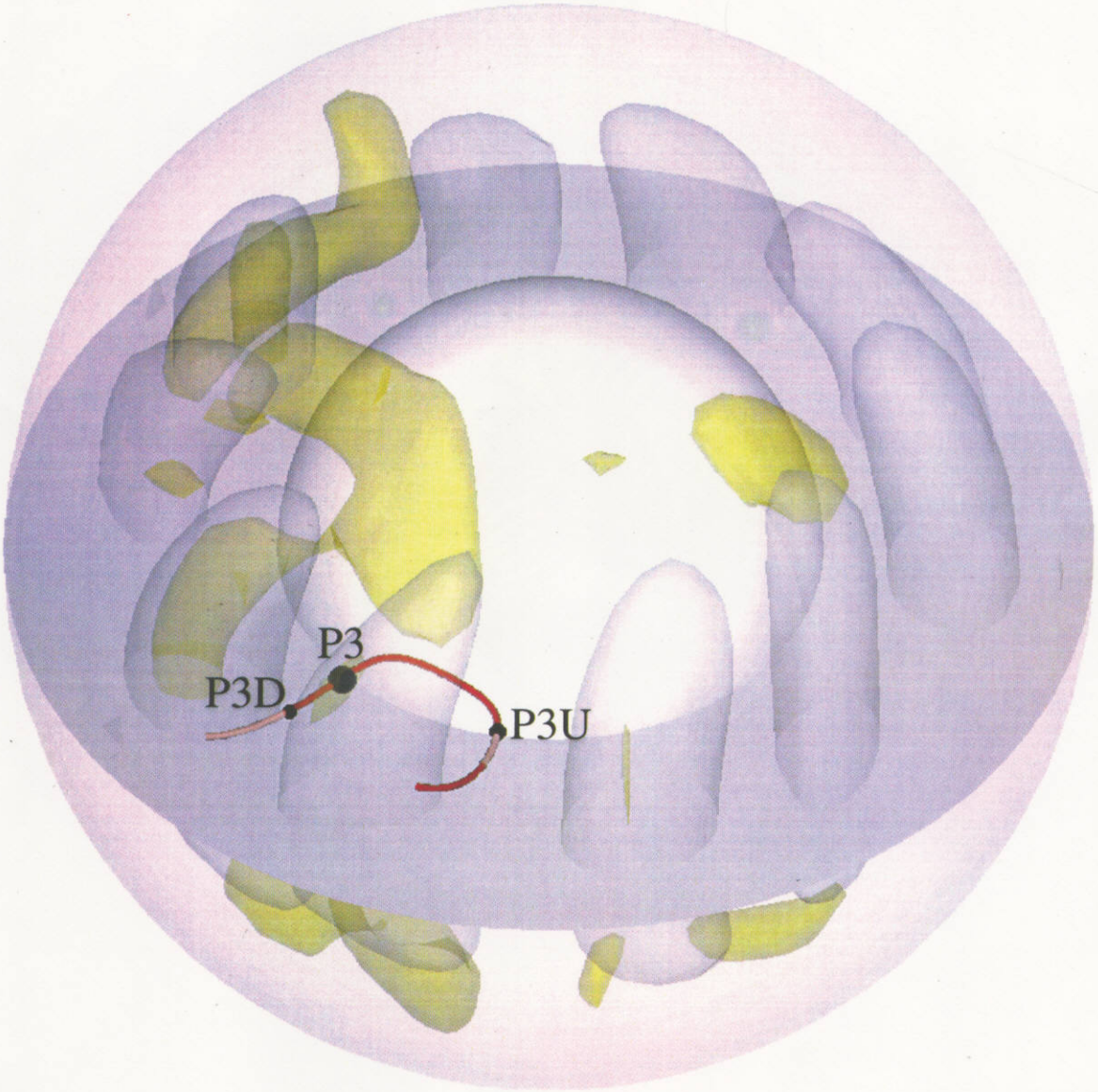

Fig. 11 (e):
H. Kitauchi and S. Kida

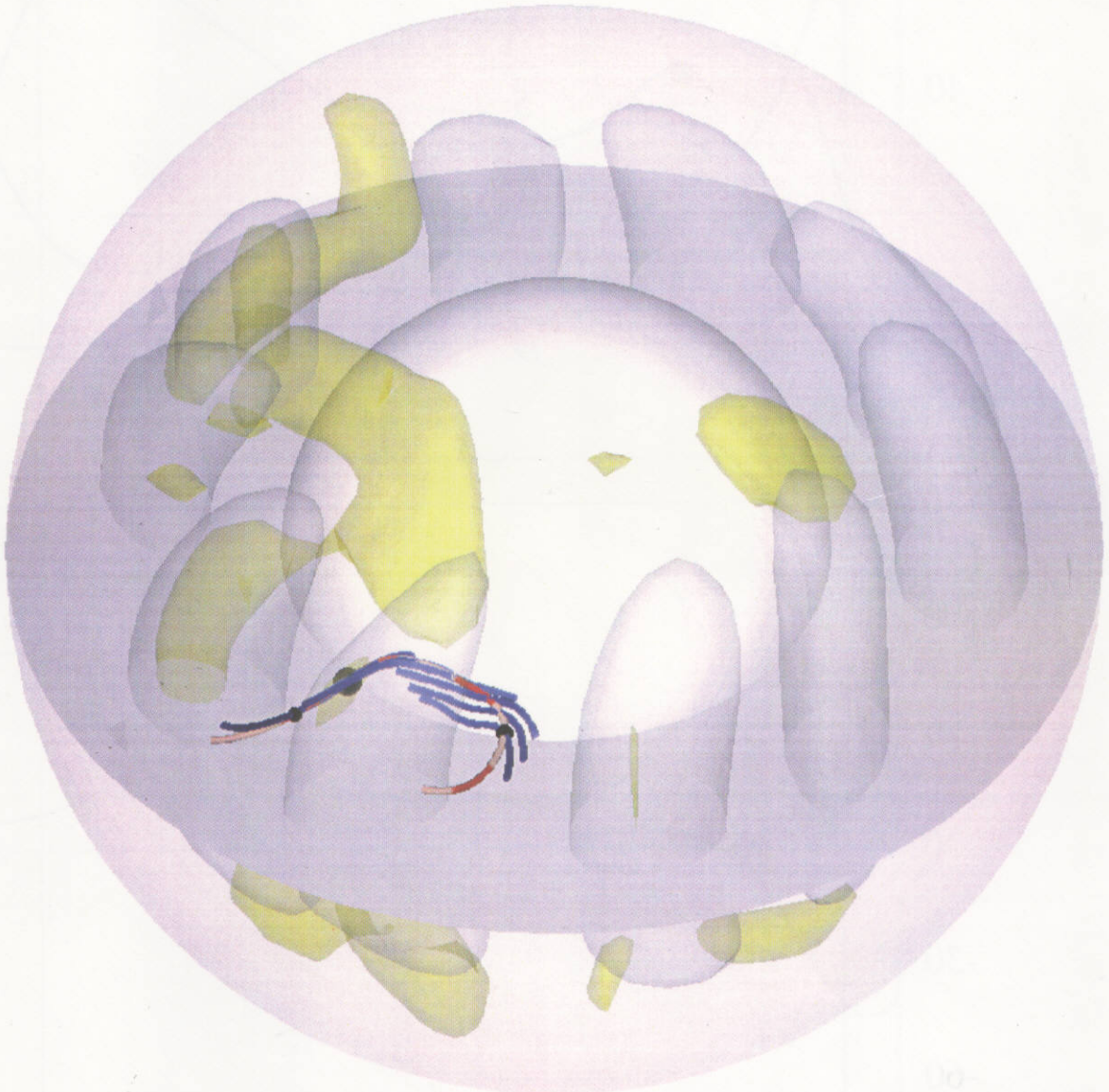

Fig. 11 (f):
H. Kitauchi and S. Kida

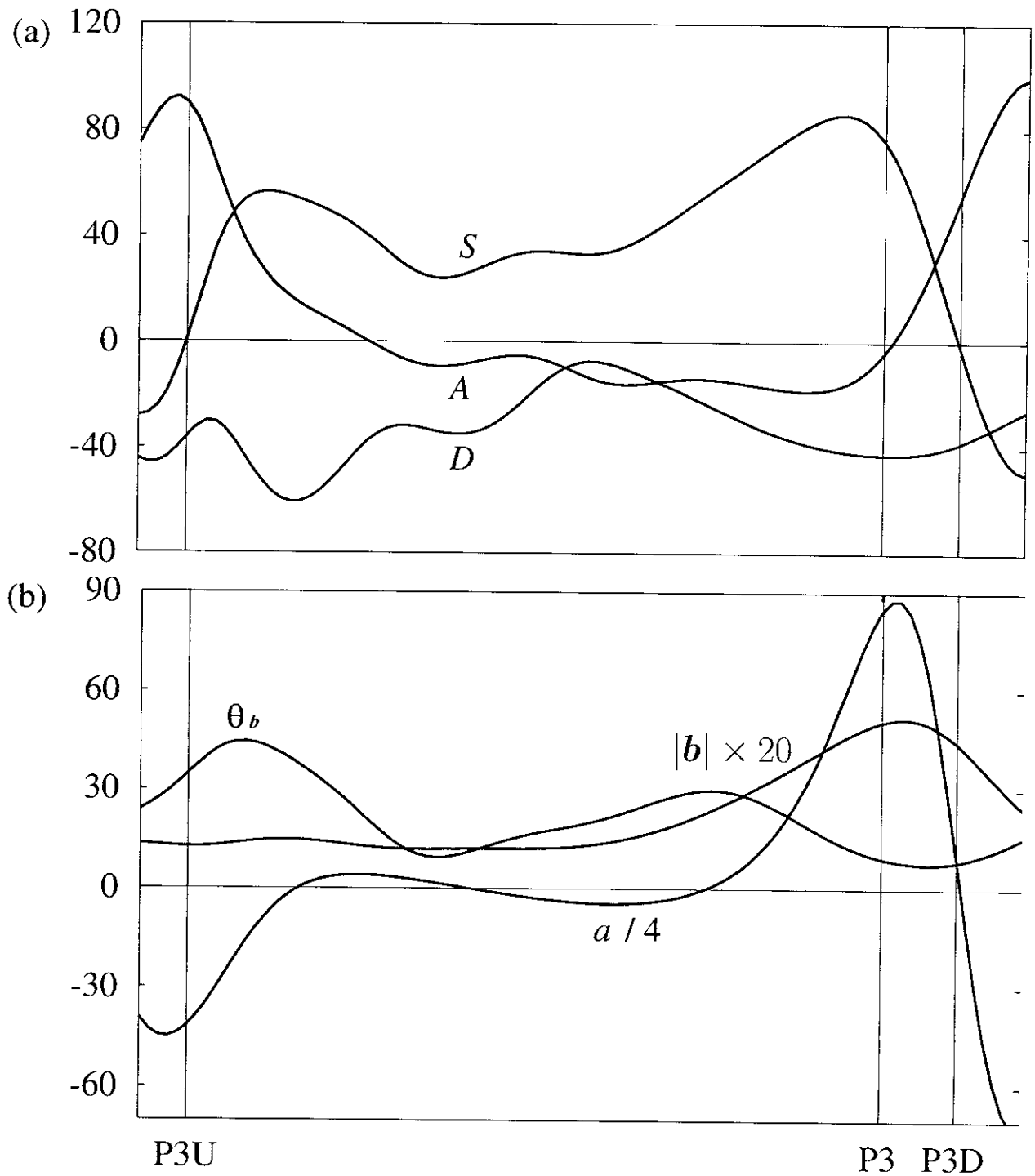

Fig. 12:

H. Kitauchi and S. Kida

Recent Issues of NIFS Series

NIFS-460 Y. Hamada, A. Fujisawa, H. Iguchi, A. Nishizawa and Y. Kawasumi,
A Tandem Parallel Plate Analyzer; Nov. 1996

NIFS-461 Y. Hamada, A. Nishizawa, Y. Kawasumi, A. Fujisawa, K. Narihara, K. Ida, A. Ejiri, S. Ohdachi, K. Kawahata, K. Toi, K. Sato, T. Seki, H. Iguchi, K. Adachi, S. Hidekuma, S.Hirokura, K. Iwasaki, T. Ido, M. Kojima, J. Koong, R. Kumazawa, H. Kuramoto, T. Minami, I. Nomura, H. Sakakita, M. Sasao, K.N. Sato, T. Tsuzuki, J. Xu, I. Yamada and T. Watari,
Density Fluctuation in JIPP T-IIU Tokamak Plasmas Measured by a Heavy Ion Beam Probe; Nov. 1996

NIFS-462 N. Katsuragawa, H. Hojo and A. Mase,
Simulation Study on Cross Polarization Scattering of Ultrashort-Pulse Electromagnetic Waves; Nov. 1996

NIFS-463 V. Voitsenya, V. Konovalov, O. Motojima, K. Narihara, M. Becker and B. Schunke,
Evaluations of Different Metals for Manufacturing Mirrors of Thomson Scattering System for the LHD Divertor Plasma; Nov. 1996

NIFS-464 M. Pereyaslavets, M. Sato, T. Shimozuma, Y. Takita, H. Idei, S. Kubo, K. Ohkubo and K. Hayashi,
Development and Simulation of RF Components for High Power Millimeter Wave Gyrotrons; Nov. 1996

NIFS-465 V.S. Voitsenya, S. Masuzaki, O. Motojima, N. Noda and N. Ohyabu,
On the Use of CX Atom Analyzer for Study Characteristics of Ion Component in a LHD Divertor Plasma; Dec. 1996

NIFS-466 H. Miura and S. Kida,
Identification of Tubular Vortices in Complex Flows; Dec. 1996

NIFS-467 Y. Takeiri, Y. Oka, M. Osakabe, K. Tsumori, O. Kaneko, T. Takanashi, E. Asano, T. Kawamoto, R. Akiyama and T. Kuroda,
Suppression of Accelerated Electrons in a High-current Large Negative Ion Source; Dec. 1996

NIFS-468 A. Sagara, Y. Hasegawa, K. Tsuzuki, N. Inoue, H. Suzuki, T. Morisaki, N. Noda, O. Motojima, S. Okamura, K. Matsuoka, R. Akiyama, K. Ida, H. Idei, K. Iwasaki, S. Kubo, T. Minami, S. Morita, K. Narihara, T. Ozaki, K. Sato, C. Takahashi, K. Tanaka, K. Toi and I. Yamada,
Real Time Boronization Experiments in CHS and Scaling for LHD; Dec. 1996

NIFS-469 V.L. Vdovin, T.Watari and A. Fukuyama,
3D Maxwell-Vlasov Boundary Value Problem Solution in Stellarator Geometry in Ion Cyclotron Frequency Range (final report); Dec. 1996

NIFS-470 N. Nakajima, M. Yokoyama, M. Okamoto and J. Nührenberg,

Optimization of M=2 Stellarator; Dec. 1996

NIFS-471 A. Fujisawa, H. Iguchi, S. Lee and Y. Hamada,
Effects of Horizontal Injection Angle Displacements on Energy Measurements with Parallel Plate Energy Analyzer; Dec. 1996

NIFS-472 R. Kanno, N. Nakajima, H. Sugama, M. Okamoto and Y. Ogawa,
Effects of Finite-β and Radial Electric Fields on Neoclassical Transport in the Large Helical Device; Jan. 1997

NIFS-473 S. Murakami, N. Nakajima, U. Gasparino and M. Okamoto,
Simulation Study of Radial Electric Field in CHS and LHD; Jan. 1997

NIFS-474 K. Ohkubo, S. Kubo, H. Idei, M. Sato, T. Shimozuma and Y. Takita,
Coupling of Tilting Gaussian Beam with Hybrid Mode in the Corrugated Waveguide; Jan. 1997

NIFS-475 A. Fujisawa, H. Iguchi, S. Lee and Y. Hamada,
Consideration of Fluctuation in Secondary Beam Intensity of Heavy Ion Beam Prove Measurements; Jan. 1997

NIFS-476 Y. Takeiri, M. Osakabe, Y. Oka, K. Tsumori, O. Kaneko, T. Takanashi, E. Asano, T. Kawamoto, R. Akiyama and T. Kuroda,
Long-pulse Operation of a Cesium-Seeded High-Current Large Negative Ion Source; Jan. 1997

NIFS-477 H. Kuramoto, K. Toi, N. Haraki, K. Sato, J. Xu, A. Ejiri, K. Narihara, T. Seki, S. Ohdachi, K. Adati, R. Akiyama, Y. Hamada, S. Hirokura, K. Kawahata and M. Kojima,
Study of Toroidal Current Penetration during Current Ramp in JIPP T-IIU with Fast Response Zeeman Polarimeter; Jan., 1997

NIFS-478 H. Sugama and W. Horton,
Neoclassical Electron and Ion Transport in Toroidally Rotating Plasmas; Jan. 1997

NIFS-479 V.L. Vdovin and I.V. Kamenskij,
3D Electromagnetic Theory of ICRF Multi Port Multi Loop Antenna; Jan. 1997

NIFS-480 W.X. Wang, M. Okamoto, N. Nakajima, S Murakami and N. Ohyabu,
Cooling Effect of Secondary Electrons in the High Temperature Divertor Operation; Feb. 1997

NIFS-481 K. Itoh, S.-I. Itoh, H. Soltwisch and H.R. Koslowski,
Generation of Toroidal Current Sheet at Sawtooth Crash; Feb. 1997

NIFS-482 K. Ichiguchi,
Collisionality Dependence of Mercier Stability in LHD Equilibria with Bootstrap Currents; Feb. 1997

NIFS-483 S. Fujiwara and T. Sato,
Molecular Dynamics Simulations of Structural Formation of a Single Polymer Chain: Bond-orientational Order and Conformational Defects; Feb. 1997

NIFS-484 T. Ohkawa,
Reduction of Turbulence by Sheared Toroidal Flow on a Flux Surface; Feb. 1997

NIFS-485 K. Narihara, K. Toi, Y. Hamada, K. Yamauchi, K. Adachi, I. Yamada, K. N. Sato, K. Kawahata, A. Nishizawa, S. Ohdachi, K. Sato, T. Seki, T. Watari, J. Xu, A. Ejiri, S. Hirokura, K. Ida, Y. Kawasumi, M. Kojima, H. Sakakita, T. Ido, K. Kitachi, J. Koog and H. Kuramoto,
Observation of Dusts by Laser Scattering Method in theJIPPT-IIU Tokamak Mar. 1997

NIFS-486 S. Bazdenkov, T. Sato and The Complexity Simulation Group,
Topological Transformations in Isolated Straight Magnetic Flux Tube; Mar. 1997

NIFS-487 M. Okamoto,
Configuration Studies of LHD Plasmas; Mar. 1997

NIFS-488 A. Fujisawa, H. Iguchi, H. Sanuki, K. Itoh, S. Lee, Y. Hamada, S. Kubo, H. Idei, R. Akiyama, K. Tanaka, T. Minami, K. Ida, S. Nishimura, S. Morita, M. Kojima, S. Hidekuma, S.-I. Itoh, C. Takahashi, N. Inoue, H. Suzuki, S. Okamura and K. Matsuoka,
Dynamic Behavior of Potential in the Plasma Core of the CHS Heliotron/Torsatron; Apr. 1997

NIFS-489 T. Ohkawa,
Pfirsch - Schlüter Diffusion with Anisotropic and Nonuniform Superthermal Ion Pressure; Apr. 1997

NIFS-490 S. Ishiguro and The Complexity Simulation Group,
Formation of Wave-front Pattern Accompanied by Current-driven Electrostatic Ion-cyclotron Instabilities; Apr. 1997

NIFS-491 A. Ejiri, K. Shinohara and K. Kawahata,
An Algorithm to Remove Fringe Jumps and its Application to Microwave Reflectometry; Apr. 1997

NIFS-492 K. Ichiguchi, N. Nakajima, M. Okamoto,
Bootstrap Current in the Large Helical Device with Unbalanced Helical Coil Currents; Apr. 1997

NIFS-493 S. Ishiguro, T. Sato, H. Takamaru and The Complexity Simulation Group,
V-shaped dc Potential Structure Caused by Current-driven Electrostatic Ion-cyclotron Instability; May 1997

NIFS-494 K. Nishimura, R. Horiuchi, T. Sato,
Tilt Stabilization by Energetic Ions Crossing Magnetic Separatrix in Field-Reversed Configuration; June 1997

NIFS-495 T. -H. Watanabe and T. Sato,
Magnetohydrodynamic Approach to the Feedback Instability; July 1997

NIFS-496 K. Itoh, T. Ohkawa, S. -I.Itoh, M. Yagi and A. Fukuyama
Suppression of Plasma Turbulence by Asymmetric Superthermal Ions; July 1997

NIFS-497 T. Takahashi, Y. Tomita, H. Momota and Nikita V. Shabrov,
Collisionless Pitch Angle Scattering of Plasma Ions at the Edge Region of an FRC; July 1997

NIFS-498 M. Tanaka, A.Yu Grosberg, V.S. Pande and T. Tanaka,
Molecular Dynamics and Structure Organization in Strongly-Coupled Chain of Charged Particles; July 1997

NIFS-499 S. Goto and S. Kida,
Direct-interaction Approximation and Reynolds-number Reversed Expansion for a Dynamical System; July 1997

NIFS-500 K. Tsuzuki, N. Inoue, A. Sagara, N. Noda, O. Motojima, T. Mochizuki, T. Hino and T. Yamashina,
Dynamic Behavior of Hydrogen Atoms with a Boronized Wall; July 1997

NIFS-501 I. Viniar and S. Sudo,
Multibarrel Repetitive Injector with a Porous Pellet Formation Unit; July 1997

NIFS-502 V. Vdovin, T. Watari and A. Fukuyama,
An Option of ICRF Ion Heating Scenario in Large Helical Device; July 1997

NIFS-503 E. Segre and S. Kida,
Late States of Incompressible 2D Decaying Vorticity Fields; Aug. 1997

NIFS-504 S. Fujiwara and T. Sato,
Molecular Dynamics Simulation of Structural Formation of Short Polymer Chains; Aug. 1997

NIFS-505 S. Bazdenkov and T. Sato
Low-Dimensional Model of Resistive Interchange Convection in Magnetized Plasmas; Sep. 1997

NIFS-506 H. Kitauchi and S. Kida,
Intensification of Magnetic Field by Concentrate-and-Stretch of Magnetic Flux Lines; Sep. 1997